

Ab initio assessment of computational thermodynamics
applied to magnetic alloys

Adie Tri Hanindriyo

Japan Advanced Institute of Science and Technology

Doctoral Dissertation

Ab initio assessment of computational thermodynamics applied to
magnetic alloys

Adie Tri Hanindriyo

Supervisor : Ryo Maezono

Graduate School of Advanced Science and Technology
Japan Advanced Institute of Science and Technology
Material Science
March, 2021

Abstract

As a highly important system both in the academic and the industrial world, there is great interest in information surrounding the Nd-Fe-B ternary system. Its importance is largely derived from one of its ternary phase, the $\text{Nd}_2\text{Fe}_{14}\text{B}$, which is used as the base compound for the most powerful permanent magnet materials available today. Alloying $\text{Nd}_2\text{Fe}_{14}\text{B}$ with other elements (substitution in atomic sites) has long been a reliable method to engineer material properties suitable for various uses. A famous example is the $\text{Nd}_2\text{Fe}_{14-x}\text{Co}_x\text{B}$ compound, which substitutes several iron (Fe) sites with cobalt (Co) in order to increase the Curie temperature (T_C), effectively increasing the working temperature of the resulting permanent magnet. Another would be the substitution of neodymium (Nd) sites with dysprosium (Dy) in order to raise the coercivity, or resistance to demagnetization by an external opposing magnetic field. Such efforts have largely produced the types of permanent magnet materials currently used in academic and industrial instruments.

Issues concerning the phase stability often arise when atomic substitution is performed, since substitution involves introducing stress and strain to the atomic crystal structure of an otherwise stable phase. Often, atomic substitution results in symmetry breaking, additional charges, and most severely destabilization of the phase. It is imperative therefore that full information regarding phase stability is obtained prior to organizing atomic substitution. Phase diagrams, therefore, are indispensable to this endeavor, and as such the CALPHAD (Calculation of PHase Diagrams) method of computational thermodynamics is highly relevant as a computational framework to draw these diagrams. The core of the CALPHAD framework is the modelling of Gibbs energy models of the competing phases in a system in order to reliably model phase transitions occurring under certain conditions (pressure, temperature, composition, *etc.*), in order to draw the phase diagram as a function of these conditions. In this work the temperature T and composition x are taken as the two degrees of freedom for the phase diagrams.

In order to ensure reliability of the models, parameters are built in to the Gibbs energy models used in CALPHAD in order to perform fitting to actual thermodynamic data of constituent phases within a system. This ensures that the resulting models accurately represent the phase stability of the competing phases, leading to a more accurate and reliable prediction of phase transitions. The data used for the fitting process has traditionally been obtained from experimental studies; however, while previous assessments of the Nd-Fe-B ternary system exist, the lack of experimental data regarding constituent phases of the Nd-Fe-B system has hampered the effort so far. In this work, we introduce *ab initio* predictions of thermodynamic properties of Nd-Fe-B to the CALPHAD assessment of the binary Nd-B system, one of the constituent systems in the Nd-Fe-B ternary system, which within the CALPHAD framework is necessary in order to investigate the ternary system as a whole.

Therefore, *ab initio* calculations of thermodynamic properties of compounds in the Nd-Fe-B ternary system and the Fe-B, Nd-B, and Nd-Fe binary systems are required to provide more complete information for CALPHAD assessment of the ternary system. The Fe-B binary system, being relatively well-investigated (due to its role in the steel industry), is excluded from the scope of this work. Two thermodynamic properties, the enthalpy of formation and the specific heat in constant pressure (C_p), are particularly relevant in the investigation, for the fitting of Gibbs energy models in CALPHAD. Density Functional Theory (DFT), as well as phonon calculation, are used as *ab initio* investigation methods to obtain the two properties for a variety of Nd-Fe-B constituent phases.

These calculations have been performed for the compounds NdB_6 , NdB_4 , Nd_2B_5 , $\text{Nd}_2\text{Fe}_{17}$ and $\text{Nd}_5\text{Fe}_2\text{B}_6$. We find that the conventional exchange correlation functional GGA (Generalized Gradient Approximation) in the DFT framework is insufficient to reliably obtain the enthalpy of formation for rare earth compounds. Instead, the Hubbard U correction based on the framework of Cococcioni and de Gironcoli (DFT+U) is employed, with values of the correction parameter U_{eff} determined from *ab initio* as well. The enthalpy of formation values obtained with the GGA+U correction shows better agreement with the available experimental data than the non-corrected GGA. We have also computed the vibrational and electronic contribution to the heat capacity (C_p) of the compounds as a function of temperature from $0 < T < 3000$ K. The results are fitted as a sum of functions from $300 < T < 3000$ K. Both the enthalpies of formation and C_p data have been utilized to reoptimize the Gibbs energy models for the binary Nd-B system, leading to a reoptimized phase diagram of the system.

Keywords: CALPHAD, *ab initio*, Nd-Fe-B, permanent magnets, phase diagram

Contents

Abstract	i
List of Figures	v
List of Tables	vi
1 Introduction	1
1.1 Background	1
1.2 Motivation	2
1.3 Problem Statements	2
1.4 Outline	3
2 Methodology	5
2.1 Density Functional Theory (DFT)	6
2.1.1 Self-consistent iteration	7
2.1.2 Hubbard U correction (DFT+U)	14
2.1.3 Forces and phonon calculation	20
2.2 CALPHAD	25
2.2.1 Gibbs energy modeling	26
2.2.2 Parameter fitting	27
2.2.3 Drawing the phase diagram	28
3 Research Objective	29
3.1 Permanent Magnets	29
3.2 Overview of the Nd-Fe-B system	30
3.2.1 Fe-B system	31
3.2.2 Nd-Fe system	31
3.2.3 Nd-B system	32
3.2.4 Nd-Fe-B system	32
4 Results and Discussion	34
4.1 Unary phases	34
4.1.1 Nd	34
4.1.2 Fe	35
4.1.3 B	35
4.2 Binary phases	36
4.2.1 NdB ₆	36
4.2.2 NdB ₄	38
4.2.3 Nd ₂ B ₅	40
4.2.4 Nd ₂ Fe ₁₇	41
4.3 Ternary phases	42

4.3.1	$\text{Nd}_5\text{Fe}_2\text{B}_6$	43
4.4	CALPHAD assessment	44
5	Conclusion	47

List of Figures

1.1	Simplified workflow of the CALPHAD method, as well as the role of <i>ab initio</i> assessments in a combined framework	3
2.1	k -point grid density convergence for the unary Boron bulk calculation	10
2.2	Fermi-Dirac function for $k_0 = 0$ and various values of σ	11
2.3	σ convergence for $\text{Nd}_2\text{Fe}_{17}$	12
2.4	Linear regressions of orbital occupation, for the 'bare' and 'converged' series, for NdB_6 Hubbard site	19
2.5	Schematic representation of LDA energy profile, the correct (piecewise constant) exact DFT energy profile for fractional occupations, and correction by Hubbard U [1]	20
2.6	Schematic representation of periodic simulation cells with indices i and atomic positions j	22
2.7	Schematic workflow of phonon calculations in this work	25
3.1	Calculated phase diagram of the Fe-B system, thermodynamic assessment by Van Ende and Jung [2]	31
3.2	Calculated phase diagram of the Nd-Fe system, thermodynamic assessment by Van Ende and Jung [2]	32
3.3	Calculated phase diagram of the Nd-B system, thermodynamic assessment by Van Ende and Jung [2]	33
3.4	An isothermal slice at 25°C of the phase diagram of the Nd-Fe-B system, thermodynamic assessment by Hallemans et al [3]	33
4.1	Unit cell of ground state Nd	34
4.2	Unit cell of ground state Fe	35
4.3	Unit cell of αB phase	35
4.4	Unit cell of NdB_6 phase	36
4.5	C_p from phonon calculation of NdB_6 , in comparison with experimental result	37
4.6	C_p from phonon calculation of NdB_6 , in comparison with estimation from the work of Bolgar et al. [4]	38
4.7	Unit cell of NdB_4 phase	38
4.8	C_p from phonon calculation of NdB_4 , in comparison with estimation from the work of Bolgar <i>et al.</i> [4]	39
4.9	Unit cell of Nd_2B_5 phase	40
4.10	C_p from phonon calculation of Nd_2B_5	41
4.11	Unit cell of $\text{Nd}_2\text{Fe}_{17}$ phase	41
4.12	C_p from phonon calculation of $\text{Nd}_2\text{Fe}_{17}$	43
4.13	Unit cell of $\text{Nd}_5\text{Fe}_2\text{B}_6$ phase	43
4.14	C_p from phonon calculation of $\text{Nd}_5\text{Fe}_2\text{B}_6$	44

4.15	Calculated C_p/T plot for NdB_6 . An unusual peak is seen around $T = 50$ K, followed by the more expected linear section.	45
4.16	Calculated phase diagram of the Nd-B binary system for $T > 300$ K, utilizing <i>ab initio</i> calculation results in this work	46

List of Tables

4.1	NdB ₆ Formation Enthalpy	36
4.2	NdB ₄ Formation Enthalpy	39
4.3	Nd ₂ B ₅ Formation Enthalpy	40
4.4	Nd ₂ Fe ₁₇ Formation Enthalpy	42
4.5	Nd ₅ Fe ₂ B ₆ Formation Enthalpy	44
5.1	Summary of formation enthalpies E_{form} obtained from first-principle calculations, with available experimental results for comparison	47

Chapter 1

Introduction

1.1 Background

The CALPHAD method (CALculation of PHase Diagrams) [5] is a mainstay in the field of Computational Thermodynamics. Its usefulness in the academic and industrial worlds is due to its capacity to model and predict phase transitions, and subsequently draw the phase diagram from simple thermodynamic information. Researchers and engineers alike frequently depend on the phase diagram in order to investigate or design materials, as it provides vital information for controlling the composition and microstructure of compounds. CALPHAD's flexibility has also allowed researchers to apply it to various systems and alloys, producing a large body of work (and a journal) dedicated to this method in the computational thermodynamics community.

Relatively recently, the field of CALPHAD has intersected with that of *ab initio* or first-principles calculation, which seeks to theoretically predict the properties of quantum systems by numerical solutions of the Schrödinger equation. The appeal of *ab initio* methods over experimental measurements are twofold: first and foremost, theoretical methods do not require as much time, energy, or financial investments as do experimental measures. Secondly, *ab initio* methods have more freedom with respect to the object of investigation than empirical methods. For example, whereas environmental factors need to be controlled very carefully in experimental conditions, *ab initio* methods simply impose different boundary conditions in calculations. CALPHAD researchers regularly include both experimental measurements and theoretical predictions in the fitting of Gibbs energy models.

A popular example is that of the Nd-Fe-B ternary system, which has among its compounds the Nd₂Fe₁₄B alloy. It is often utilized, due to its high magnetisation, as a base alloy for the strongest permanent magnets. [6] In practice however, it is often alloyed with other compounds in order to improve its working performance. A well-known example is micro-alloying with Dy [7] in order to raise coercivity. These improvements require reliable thermodynamic data and reliable modeling in order to accurately predict phase transitions and stability. There is however little experimental information regarding constituent systems (and the phases contained) of Nd-Fe-B system, which is where *ab initio* has a role to play.

Density Functional Theory (DFT) is regularly utilized among researchers in *ab initio* calculation field due to the balance of feasibility and reliability it brings to the table. [8] It has been used in previous works to predict from first-principles thermodynamic properties of compounds which led to reoptimization of the Gibbs energy models in CALPHAD. [9] In this manner, the DFT-CALPHAD framework has been successfully utilized to plot the phase diagram of a system from first-principles. This approach has served to provide a more complete view of

materials which have traditionally been inhibited by experimental constraints (phases either metastable or hard to synthesize).

1.2 Motivation

CALPHAD, in essence, is a framework within computational thermodynamics for modelling phase transitions using Gibbs energy models using parameters fitted to thermodynamic data of a system's constituent phases. The fitting process hinges upon a reliable collection of these data, and often the user of CALPHAD has to prioritize one data point over another due to measurement inaccuracies or other uncertainties inherent to the methodology. Experts have classically used a weighting scheme to take into account the reliability of available thermodynamic data; the more reliable the data, the larger weight is assigned to it during the fitting process, and from that follows a more reliable Gibbs energy model and phase diagram. While more reliable data desired as a matter of course, generally speaking, it is desirable to provide as much data points as possible in order to allow for personal discernment from the CALPHAD user.

In this sense, DFT stands to provide valuable, reliable input to the parameter fitting process in CALPHAD. This is true especially as investigations in the academic field start to move toward unknown territory (machine learning, materials searching) where *ab initio* theoretical predictions are practically vital as experimental measurements for a large number of compounds become increasingly unfeasible. There is ample motivation to provide a robust framework of first-principles investigation that is able to be applied rigorously across a large number of systems while maintaining a reasonable computational cost. Therefore, first-principles frameworks such as DFT-CALPHAD are of great value to the field of computational thermodynamics and materials science alike.

Case studies for the application of these frameworks are ideally well-suited to their advantages over classical approaches to CALPHAD. The Nd-Fe-B system is chosen due to the lack of available thermodynamic data with regards to some of the constituent phases and systems. For example, while the constituent Fe-B binary system is rather well-documented and well-known [10, 11], the Nd-Fe and Nd-B binary systems are less well-investigated. The same can be said for the ternary compounds within the system itself, making the Nd-Fe-B system a good case where first-principles investigation can bring much-needed data to improve the Gibbs energy modeling. Seeing its industrial and economic importance as well, it also stands to show how first-principles frameworks can more widely impact the world beyond academic fields.

1.3 Problem Statements

Concisely put, the method of CALPHAD involves construction of Gibbs energy models, the optimization or fitting of parameters within these models, and the use of said models to computationally predict phase transitions across a range of environmental variables (such as temperature T , pressure P , or composition). In order to build reliable Gibbs energy models for a system, the fitting process requires parameters within the models to be optimized according to phase equilibria and thermodynamic properties of constituent compounds within the system. As shown in Figure 1.1, thermodynamic properties of compounds can be predicted by *ab initio* methods, which can subsequently be utilized in the parameter fitting of Gibbs energy models. Meanwhile, the Gibbs energy contribution of unaries are generally taken from the unary database in CALPHAD, forming the first mathematical terms of the Gibbs energy models.

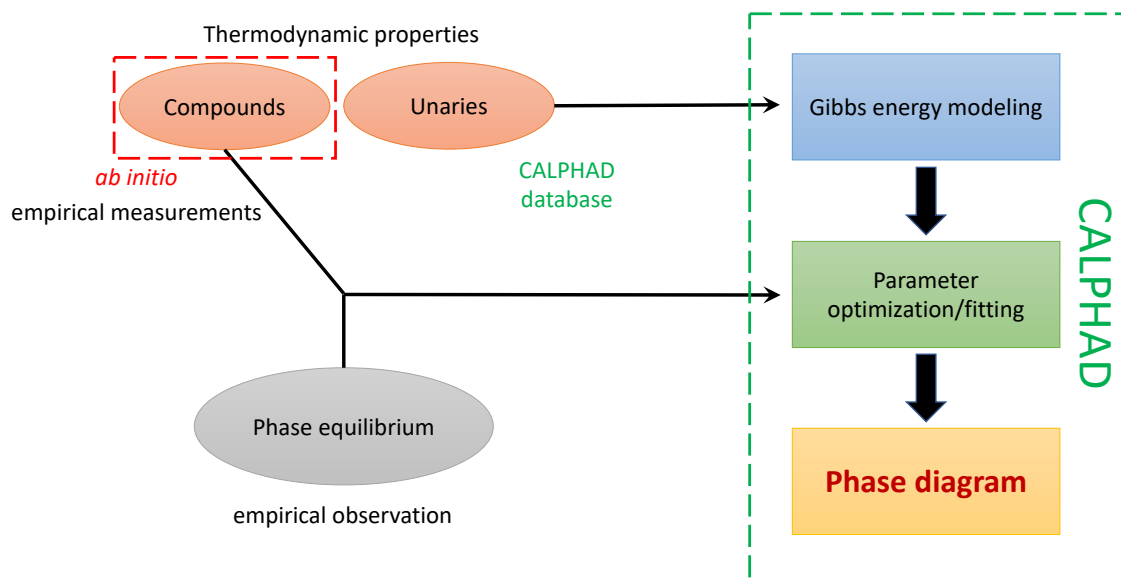


Figure 1.1: Simplified workflow of the CALPHAD method, as well as the role of *ab initio* assessments in a combined framework

The DFT-CALPHAD framework is structured around this general workflow, with *ab initio* methods focusing on calculations of thermodynamic properties relevant to the fitting of parameters in CALPHAD. These properties are generally relevant toward either the enthalpy H or the entropy S terms for the Gibbs energy:

$$\Delta G = \Delta H - T\Delta S \quad (1.1)$$

Enthalpy of formation (ΔH_f) of the constituent phases provide a convenient dataset for the optimization of the Gibbs energy parameters related to enthalpy, while entropy may be fitted against the specific heat with respect to temperature ($C_p(T)$). Meanwhile, CALPHAD work focuses on the creation of robust Gibbs energy models and effective optimization of parameters within the models, focusing on the interaction between Gibbs energy contribution of phases within the system. Validation involves comparison of the results with available data generally cited from previous empirical and theoretical works.

1.4 Outline

This work is divided into 6 chapters.

- Chapter 1: Introduction serves as an introduction to the background of this work, as well as the motivation behind this project. It also contains a summary of the workflow, the scope of the research, and an outline of this work
- Chapter 2: Methodology enumerates the existing literature concerning the methodologies

used in this work, mainly that of the DFT and CALPHAD methods. Core principles are described, as well as unique considerations taken within this work (as well as the reasoning involved)

- Chapter 3: Research Objective discusses the Nd-Fe-B system as the objective of this work, including its application and available literature on the system
- Chapter 4: Results and Discussion details the results obtained within the course of research, as well as discussion on some points regarding the results
- Chapter 5: Conclusion serves as a brief summary of Chapters 2, 3, and 4, concisely expressing the main points, results, and conclusion of this work

Chapter 2

Methodology

One of the core principles of Quantum Mechanics is that quantum particles, unlike classical objects, do not behave in a fully deterministic manner. Uncertainty, it seems, is built into the quantum world, represented by the Heisenberg uncertainty principle. However, it is still possible to predict (to a certain extent) the behavior of quantum particles by way of the Schrödinger equation:

$$\frac{-\hbar^2}{2m}\nabla^2\Psi(\mathbf{r},t) + V(\mathbf{r})\Psi(\mathbf{r},t) = i\hbar\frac{\partial\Psi(\mathbf{r},t)}{\partial t} \quad (2.1)$$

with the two terms on the left being kinetic and potential energies, respectively. Practically, the Schrödinger equation is often separated into the time-dependent (t) and time-independent (\mathbf{r}) forms. As quantum transitions often take place in a fraction of a second, most of the time it is much more important to obtain the steady-state solution. More often than not, physicists contend with the time-independent Schrödinger equation (colloquially abbreviated as TISE):

$$\frac{-\hbar^2}{2m}\nabla^2\psi(\mathbf{r}) + V(\mathbf{r})\psi(\mathbf{r}) = E\psi(\mathbf{r}) \quad (2.2)$$

as an eigenvalue problem with the Hamiltonian operator \hat{H} , again consisting of the kinetic and potential terms as:

$$\left(\frac{-\hbar^2}{2m}\nabla^2 + V(\mathbf{r})\right)\psi(\mathbf{r}) = \hat{H}\psi(\mathbf{r}) = E\psi(\mathbf{r}) \quad (2.3)$$

Analytic solutions are difficult to come by, however, as the effort required to solve Equation 2.3 scales poorly with number of quantum particles. For a quantum system with N quantum particles, the TISE shifts into a $3N$ -dimension differential equation, which is almost impossible to solve analytically. This is the main reason why analytic solutions are only available for a select few cases where only several particles in simple potentials are involved (particle-in-a-box, harmonic oscillator, hydrogen and helium atoms), whereas even for the simplest molecules they may be just out of reach.

While there are already reliable methods to find numerical solutions of $\psi(\mathbf{r})$ for second-order differential equations, the computational effort required scales very poorly with the number of particles. Therefore, any methodology aiming to solve the TISE necessarily include approximations which must aim to balance feasibility and reliability to some degree. First-principles or *ab initio* methods were developed with the main goal to seek out numerical solutions to the Schrödinger equation efficiently, without relying on parameters with values taken from empir-

ical observations (unlike semi-empirical methods). Growth in this field has led to successful theoretical calculations of systems of up to $N = 10000$ particles, which has played an instrumental role in physics, chemistry, and microbiology (simulations of DNA [12, 13], for example).

In order to reduce the complexity of the many-body Schrödinger equation, it is useful to consider the massive difference in kinetic energy between electrons and nuclei. The large difference in mass between the two particles mean that it is possible to approximate quantum systems as comprised of high velocity electrons around stationery nuclei. Essentially, the quantum system with M nuclei is seen as a sequence of potential energy surfaces $E(\mathbf{R}_1, \mathbf{R}_2, \dots, \mathbf{R}_M)$ at different nuclei locations $\mathbf{R}_1, \mathbf{R}_2, \dots, \mathbf{R}_M$. This is a famous approximation know as the Born-Oppenheimer approximation [8], which neatly separates the electronic and nucleic terms within the Hamiltonian:

$$\left(\frac{-\hbar^2}{2m} \sum_{i=1}^N \nabla_i^2 + \sum_{i=1}^N \sum_{j<i}^N V(\mathbf{r}_i, \mathbf{r}_j) + \sum_{i=1}^N U(\mathbf{r}_i : \mathbf{R}_1, \mathbf{R}_2, \dots, \mathbf{R}_M) \right) \psi(\mathbf{r}) = E\psi(\mathbf{r}) \quad (2.4)$$

with $V(\mathbf{r}_i, \mathbf{r}_j)$ the potential from interacting electrons i and j and $U(\mathbf{r}_i : \mathbf{R}_1, \mathbf{R}_2, \dots, \mathbf{R}_M)$ the potential energy surface with respect to nuclei positions (electron-ion and ion-ion interactions). Most *ab initio* methods make use of the Born-Oppenheimer approximation and consider only electrons as the quantum particles in the system, separating the electron-electron, electron-ion, and ion-ion potential energy terms in the Hamiltonian.

2.1 Density Functional Theory (DFT)

Density Functional Theory (DFT) was developed from the pioneering works of Hohenberg, Kohn, and Sham [14, 15] in the 1960's and has since been proven to be one of the most powerful tools available to physicists among other *ab initio* methods. Hohenberg and Kohn's work [14] produced conclusions referred to today as the Hohenberg-Kohn theorems, which form the core principles of DFT. The first theorem, as summarized in the book "Density Functional Theory: A Practical Introduction" by Sholl and Steckel:

"The ground-state energy from Schrödinger's equation is a unique functional of the electron density." [8]

states that it is possible to map distributions of electron density $n(\mathbf{r})$ to unique values of ground-state energy E . In other words, for any quantum system, there must exist a functional of electron density which produces the ground-state energy $E[n(\mathbf{r})]$. Practically speaking, this is a very convenient fact as the many-body problem of finding the solution of $E(\mathbf{r}_1, \mathbf{r}_2, \dots, \mathbf{r}_N)$ for a quantum system of N electrons can theoretically be perfectly converted to that of finding the true density functional $E[n(\mathbf{r})]$, greatly reducing the complexity from a $3N$ -dimensional differential equation to a 3-dimensional one ($\mathbf{r} = (r_x, r_y, r_z)$). Coupled with the second theorem, again as summarized by Sholl and Steckel:

"The electron density that minimizes the energy of the overall functional is the true electron density corresponding to the full solution of the Schrödinger equation." [8]

means that it is theoretically possible to obtain the solution to the Schrödinger equation by variationally minimizing the density functional $E[n(\mathbf{r})]$.

Kohn and Sham would later discover the Kohn-Sham equation [15], which converts the many-body Schrödinger equation into a system of non-interacting electrons represented by single-particle wavefunctions $\psi_i(\mathbf{r})$:

$$\left(\frac{-\hbar^2}{2m} \nabla^2 + V(\mathbf{r}) + V_H(\mathbf{r}) + V_{XC}(\mathbf{r}) \right) \psi_i(\mathbf{r}) = \epsilon_i \psi_i(\mathbf{r}) \quad (2.5)$$

The potential terms from the many-body Hamiltonian is split into three parts: the nuclei-electron potential $V(\mathbf{r})$, the Hartree potential (electron-electron) $V_H(\mathbf{r})$, and the exchange-correlation functional $V_{XC}(\mathbf{r})$. The Kohn-Sham equation is in practice solved iteratively with a fraction of the effort it takes to solve the full many-body Schrödinger equation. The reliability of this framework largely relies on how exact the density functional $E[n(\mathbf{r})]$ is to the *true* form of the density functional, largely represented by the “unknown” form of the exchange-correlation functional $V_{XC}(\mathbf{r})$.

To summarize the fundamental principles of DFT, the electron density $n(\mathbf{r})$ can be uniquely mapped to the ground state energy E , forming the density functional $E(n(\mathbf{r}))$. By variational minimization of the $E(n(\mathbf{r}))$, it is possible to obtain the true electron density $n(\mathbf{r})$ of the quantum system. Finally, by converting the many-body problem of the Schrödinger equation to a series of single-particle Kohn-Sham equations, computational solving of the many-body problem becomes feasible.

From the Hohenberg-Kohn theorem, it is proven that the conversion from the many-body Schrödinger equation to the Kohn-Sham equations can be exact (without error). However, practically speaking, this exact conversion is not achievable due to forms of electron interaction not properly accounted in the Kohn-Sham equation. The term $V_{XC}(\mathbf{r})$ in the Kohn-Sham equation is the exchange-correlation (XC) functional which describes exchange interactions and electron correlation, and represents the “unknown” mathematical forms of electron interaction from the many-body problem.

2.1.1 Self-consistent iteration

Beginning with an initial guess of the electronic density $n(\mathbf{r})$, the Kohn-Sham equations are solved by matrix diagonalization in order to produce the single-particle eigenfunctions $\psi_i(\mathbf{r})$. The computation results are used to re-calculate the new electronic density $n^*(\mathbf{r})$, which is then compared with the initial guess $n(\mathbf{r})$. If the difference between the two electronic densities exceed a certain tolerance value, the calculation enters a new iteration by utilizing some form of mixing between the initial and new electron densities. The loop proceeds in the same manner until the difference between old and new densities falls below the tolerance value, in which case the density is said to be ‘self-consistent’ and the loop ends, resulting in the electron density $n(\mathbf{r})$ corresponding to the true ground state electronic density.

Despite the seeming simplicity of the core process of DFT, practically there are deeper considerations that must be taken beyond the choice of the exchange-correlation functional (while being an important factor in and of itself). In fact, these considerations contribute significantly to the reliability of DFT for any certain system, and is quite common to be the source of significant error when neglected. These basic practical considerations are described in the book by Sholl and Steckel [8] and briefly discussed here:

Basis set

Within quantum mechanics, the state of quantum particle is embodied within a mathematical function known as the wavefunction. They are typically represented by the basis set, which is a set of basis functions representation of the wavefunction. Expanding the basis set allows the wavefunction to be more rigorously represented, and more complexity within its behavior captured in its representation. Practically, physicists and chemists would choose a set of basis functions that best model their system and the extent of the basis set expansion. The complete basis set (CBS) limit is defined as the extent of basis set expansion which is equivalent to an infinitely large basis set, usually obtained from extrapolation from multiple sizes of basis set. Realistically however, a tolerance value is generally adopted in order to balance computational feasibility and accuracy; for example, at the level of chemical accuracy (around 1 kcal/mol).

Plane-wave basis set is often utilized in systems with periodic boundary conditions, fully taking advantage of the periodic nature of plane waves. Therefore, calculations of bulk compounds (infinitely periodic in 3D) or surfaces (periodic in 2D) often use plane-wave basis set to represent the electronic wavefunction. Equation 2.6 shows a general plane-wave basis set expanded in wavevector \mathbf{k} , arising from the Fourier transform from real-space coordinates \mathbf{r} :

$$\psi_i(\mathbf{r}) = \sum_{\mathbf{k}} c_i(\mathbf{k})e^{i\mathbf{k}\cdot\mathbf{r}} \quad (2.6)$$

The term ‘‘cutoff energy’’ of plane-wave basis set is used to set the extent of the basis set expansion. Higher energy plane waves (with larger wavevector \mathbf{k}) represent diminishingly small contributions (in general) to the overall wavefunction. In computational calculations, the contribution of plane waves beyond the cutoff energy E_{cut} is deemed insignificant to the result of calculation (to within a tolerance value).

$$E_{\text{cut}} = \frac{\hbar^2}{2m} |\mathbf{k}_{\text{max}}|^2 \quad (2.7)$$

The cutoff energy E_{cut} introduces a limit to the expansion in Equation (2.6), limiting the basis set to functions defined in Equation 2.8.

$$\psi_i(\mathbf{r}) = \sum_{\mathbf{k} < \mathbf{k}_{\text{max}}} c_i(\mathbf{k})e^{i\mathbf{k}\cdot\mathbf{r}} \quad (2.8)$$

First-principles calculation of bulk structure of compounds make up the overwhelming majority of the calculations performed within this work. As such, the plane-wave basis set is chosen to represent the periodic electronic wavefunctions.

Reciprocal space

Taking full advantage of the periodic nature of bulk or surface calculations, it is computationally very efficient to perform a Fourier transform on real space coordinates and perform calculations over the frequency domain (over the wavevectors \mathbf{k} instead of position vectors \mathbf{r}). The resultant coordinates from the Fourier transform is referred to as the reciprocal space or the \mathbf{k} -space. It is not a concept alien to materials science, as other branches within the field (X-ray diffraction, for instance) also utilizes the reciprocal space to take advantage of crystal periodicity.

The lattice vectors of the crystal cell \mathbf{a}_1 , \mathbf{a}_2 , and \mathbf{a}_3 is redefined in reciprocal space by Fourier transformation. It is notable that the real space and reciprocal space lattice vector lengths are

inversely proportional; a longer real space lattice vector is transformed into an inversely smaller reciprocal lattice vector according to Equation 2.9.

$$\begin{aligned}
 \mathbf{b}_1 &= 2\pi \frac{\mathbf{a}_2 \times \mathbf{a}_3}{\mathbf{a}_1 \cdot (\mathbf{a}_2 \times \mathbf{a}_3)} \\
 \mathbf{b}_2 &= 2\pi \frac{\mathbf{a}_3 \times \mathbf{a}_1}{\mathbf{a}_2 \cdot (\mathbf{a}_3 \times \mathbf{a}_1)} \\
 \mathbf{b}_3 &= 2\pi \frac{\mathbf{a}_1 \times \mathbf{a}_2}{\mathbf{a}_3 \cdot (\mathbf{a}_1 \times \mathbf{a}_2)}
 \end{aligned} \tag{2.9}$$

A primitive cell in reciprocal space is known as the Brillouin zone; the smallest volume which contains all the information necessary to reproduce crystal periodicity in 3 dimensions. Needless to say, it is computationally most efficient to work within the Brillouin zone (akin to utilizing the primitive cell as the minimum volume in real space). Practically, the irreducible Brillouin zone (IBZ) is obtained by taking advantage of crystal symmetry in the Brillouin zone in order to further minimize the computational effort.

In computation, numerical solutions of integrals over variable x is approximated as sums over discrete values of x . In the same way, integrations over wavevectors \mathbf{k} is discretized as summations over a selection of points in the Brillouin zone (oft referred to as k -points). The concept of k -mesh is very important in *ab initio* calculations as a grid of k -points in the reciprocal space, over which summations are performed to numerically solve analytic integrals. Due to the nature of the reciprocal space, each k -point may be weighted differently depending on its significance to the crystal structure and crystal symmetry.

The Monkhorst-Pack [16] scheme of k -mesh generation is often used for identifying relevant k -points in the Brillouin zone. There is a computational need to carefully balance the density of the k -mesh. While denser k -mesh is ideal in order to more reliably approximate integrals over the IBZ, it also increases the computational cost to calculate over a larger set of k -points. Where high frequency oscillations of the wavefunction occur (higher energy terms in the basis set), a denser collection of k -points is also required. As with the cutoff energy E_{cut} , it is desirable to increase the k -mesh density up to a certain point above which increasing the number of k -points does not significantly impact the accuracy of calculations.

Parameter convergence

The cutoff energy E_{cut} and k -mesh density are two important parameters which determines the cost and accuracy of DFT calculations. It is therefore standard practice to measure the convergence of at least both of these parameters before starting a production (actual) calculation. Often times the ground state energy of the quantum system (colloquially the ‘‘Total energy’’) is used as a measurement for convergence of calculation results with respect to calculation parameters.

Figure 2.1 shows an example of total energy convergence with respect to k -mesh density for the unary Boron ground state. Several quick single-point calculations are performed, with differing $M \times M \times M$ k -mesh (M points along a reciprocal lattice axis), and the change in the total energy is apparent. Adopting a tolerance value of 1 mRy (well below the chemical accuracy of 1 kcal/mol \approx 3 mRy) it can be seen that the value of $M = 4$ is enough to achieve convergence below the tolerance value. The addition of M above $M = 4$ does not contribute significantly to the total energy and as such merely serves to increase the computational cost.

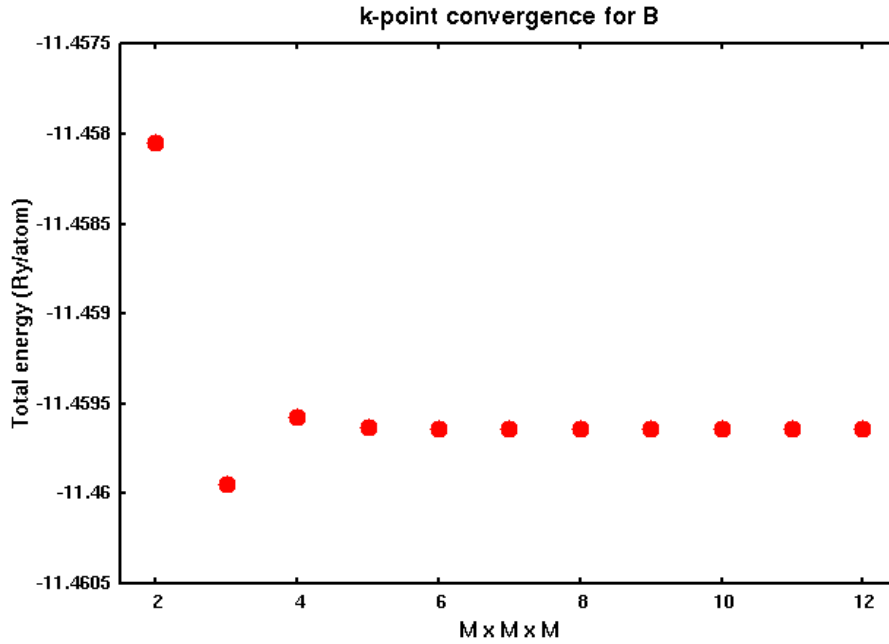


Figure 2.1: k -point grid density convergence for the unary Boron bulk calculation

For a crystal structure with nonequal lattice vector lengths, the k -mesh grid should follow the inverse proportion of real space and reciprocal lattice vectors. For example, a tetragonal crystal structure with real space lattice vector length ratio of 2:1:1 should translate to a k -mesh of $M \times 2M \times 2M$. The k -mesh grid is further reduced by Brillouin zone symmetry in order to minimize as much as possible the number of k -points.

Calculation parameters are converged on-by-one before production calculations by taking an arbitrarily reliable value for unconverged parameters and converging one in particular, to reliably track the convergence with respect to one parameter in particular. Parameter convergence for the cutoff energy works in the same way, tracking the total energy convergence with respect to E_{cut} value.

Smearing

Smearing is an artificial imposition on the occupation of electron states in electronic structure calculations in order to significantly reduce computational cost. It is important for metallic systems where the valence band structure often crosses the Fermi surface, which can lead to inaccurate results of calculations of material properties. Most ground state properties rely on integrals or discrete sums over occupied electron states. In metallic systems, where occupation of electron states may sharply increase or decrease where band crossings of the Fermi surface occur, the material properties may not be reliably calculated unless a dense k -mesh is adopted. This sharp transition is akin to including a step function in integrals for bands near the Fermi surface and leads to a dramatic fluctuation in the total energy as well.

The practical effect of this fluctuation of total energy is that convergence of DFT calculations for metallic systems is notoriously difficult to achieve without a dense k -mesh. In order to reduce the number of k -points needed to reliably calculate the electronic structure, smearing is introduced as a measure to alleviate the sharp transition of occupation. Smearing functions effectively introduce slopes instead of step functions, artificially easing the difficulty in obtaining

a self-consistent solution for the charge density $n(\mathbf{r})$. Equation 2.10 shows an example of the Fermi-Dirac smearing function:

$$f\left(\frac{k - k_0}{\sigma}\right) = \frac{1}{\exp\left(\frac{k - k_0}{\sigma}\right) + 1} \quad (2.10)$$

as a sloped step function at $k = k_0$ depending on the value of σ . Figure 2.2 shows the Fermi-Dirac smearing function with various values of smearing parameter σ . It can be seen that larger values of σ increases the slope of the function at $k = k_0$.

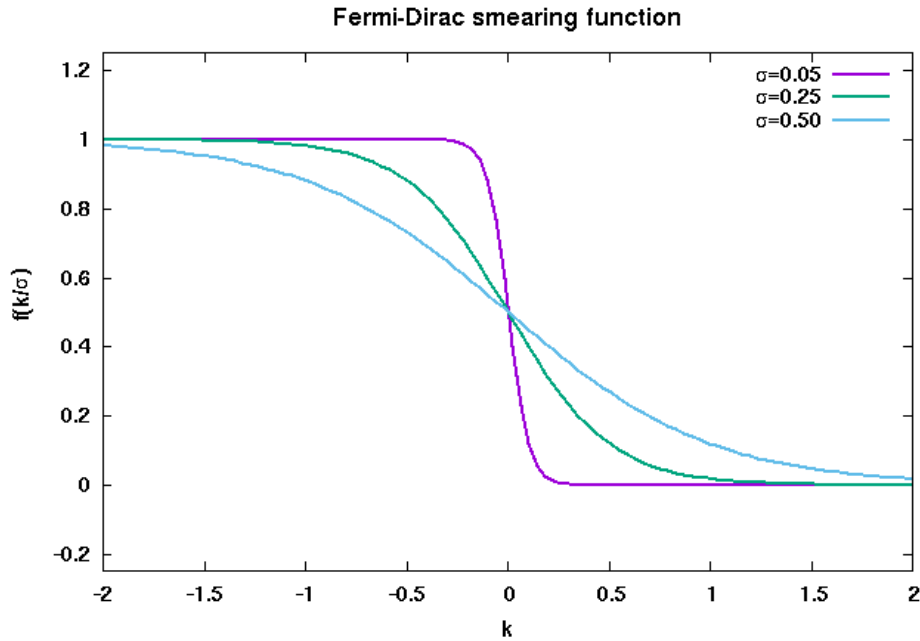


Figure 2.2: Fermi-Dirac function for $k_0 = 0$ and various values of σ

Various smearing functions exist and within this work, the Marzari-Vanderbilt cold smearing [17] is used to broaden the occupation by convolution with a delta function:

$$\tilde{\delta}(x) = \frac{2}{\sqrt{\pi}} e^{-\left[x - \left(\frac{1}{\sqrt{2}}\right)\right]^2} (2 - \sqrt{2}x) \quad (2.11)$$

As an artificial imposition on the wavefunction, it is desirable to limit the smearing parameter σ to as small as possible to preserve the accuracy of the calculation. Practically, it is converged in the same way as cutoff energy and k-mesh density, as shown in Figure 2.3.

In this example, it is shown that values of smearing parameter σ beyond 0.03 Ry more significantly affects the total energy, which limits the smearing parameter to 0.03 Ry to help the self-consistent requirement.

Pseudopotential

An early conclusion in chemistry is that elements in the same periodic table group tend to behave in a similar chemical manner. The grouping of elements in the periodic table reflects the valence electrons in an atom which, as a result of being weakly bonded to the nucleus, are easily transferred or shared between atoms, forming chemical bonds (ionic, covalent). In short,

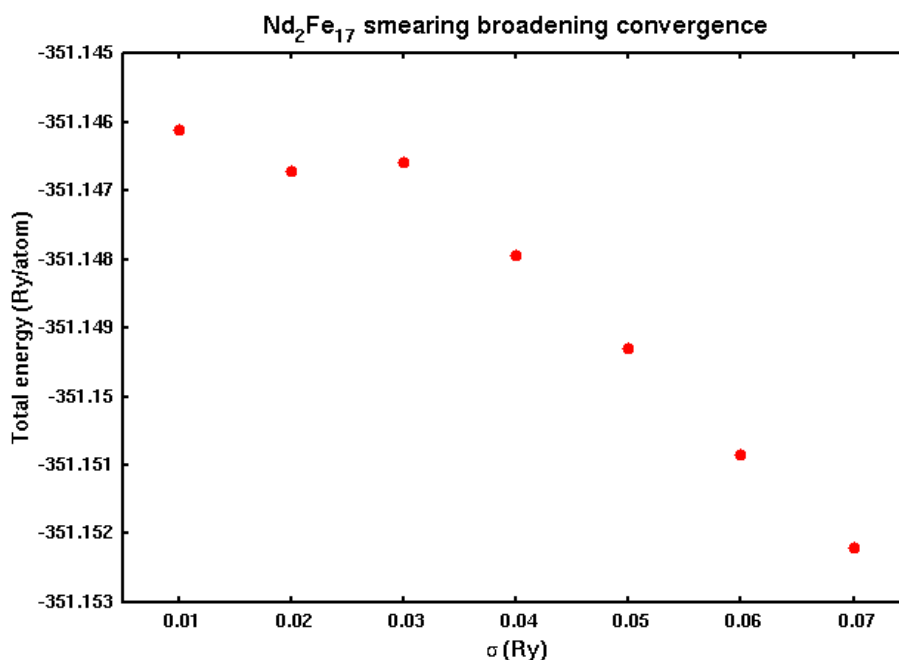


Figure 2.3: σ convergence for Nd₂Fe₁₇

valence electrons carry far more significance in chemical bonding than the more tightly bound core electrons.

The field of quantum chemistry takes advantage of this physical fact by employing pseudopotentials in place of core electrons. These pseudopotentials reproduce the screening of valence electrons by core electrons, effectively removing the need to include core electrons in electronic structure calculations. Pseudopotentials are constructed so that up to a cutoff radius of r_c from the nucleus, the wavefunction is approximated by a simpler smoothed function which reproduces the behavior of a core electron, and simply recreates the valence electron wavefunction beyond the cutoff radius. The advantage of this “frozen-core” approximation is twofold:

- Removing the core electrons from consideration is vital for calculations of heavy elements, for which all-electron calculations (without pseudopotentials) are computationally unfeasible. This is also true for large quantum systems where all-electron calculations scale very poorly with the number of particles.
- Higher energy core electrons possess rapidly oscillating wavefunctions near the nucleus, which must be represented by higher expansions in the basis set. By excluding core electrons from consideration, the expansion of basis set can be stopped in lower energies, again reducing the computational cost of electronic structure calculations greatly.

Various forms of pseudopotentials exist with its own strengths and weaknesses. Two prominent types of pseudopotentials are the norm-conserving (NC) pseudopotentials and the projector augmented-wave (PAW). Norm-conserving pseudopotentials [18,19] are so called due to the requirement of preserving the charge density of the all-electron core within the cutoff radius. While ensuring good transferability, this also requires higher energy expansions of the basis set, which is referred to as the “hardness” of the pseudopotential. Meanwhile, the projector augmented-wave pseudopotentials [20,21] are softer in comparison and much more commonly used recently due to their efficiency.

Exchange-correlation potentials

As previously mentioned the exchange-correlation functional is the single most important approximation within DFT. This is due to the unknown form of the exchange-correlation functional which must be approximated, since only the *existence* of the true exchange-correlation functional has been mathematically proven. In this sense, DFT can be said to be *exact*, that there is an exact form of the exchange-correlation functional which minimizes the ground state energy and reproduces the real ground state charge density. It can be said that the Hamiltonian is split between the “known” and “unknown” parts of DFT, with the kinetic, electron-electron, and electron-nucleus potentials representing the “known” physical interactions. The exchange-correlation functional represents the practically “unknown” factor in DFT, and is approximated by various functional forms, some of which might work well for some systems and not for others. The choice of exchange-correlation functional is in a sense the most important choice on the part of the physicist in determining the reliability of DFT calculations.

One of the earliest and simplest forms of exchange-correlation functional is the Local Density Approximation (LDA) [22], constructed from calculations of the homogeneous electron gas (jellium model). It is a functional of the local density $n(\mathbf{r})$ at a point in space, $V_{XC}(\mathbf{r}) = V_{XC}^{LDA}[n(\mathbf{r})]$, from which it earned its name. Despite its simplicity, it has surprisingly performed well for a wide range of systems, especially where electron density resembles that of the jellium model. Another form of the exchange-correlation functional is the Generalized Gradient Approximation (GGA) [23], which beyond the electron density, also takes into account the gradient of electron density. In practice, GGA is more reliable than LDA for systems where sharp gradients of $n(\mathbf{r})$ exist, such as surfaces and semiconductors. As such, GGA exchange-correlation functional is used in this work for DFT calculations.

The reliability of both LDA and GGA exchange-correlation functionals, while perfectly good for a wide variety of systems, is not perfectly applicable on all quantum systems. There are famous examples within the *ab initio* community for which neither LDA nor GGA give the correct solution, for example transition metal oxides (such as NiO [24] and graphene [25]). Practically, physicists employ different exchange-correlation functionals and different corrections to take into account the strengths and weaknesses of each type, choosing one which best fits the system. A well known case of this are the strongly correlated class of materials, for example, transition metal oxides and rare-earth elements with localized $4f$ electrons, where electron exchange and correlation serve a more significant role in their properties. As a result, conventional exchange-correlation functionals have been proven to be unable to properly predict properties of these materials.

Other forms, such as hybrid exchange-correlation functionals, have been successfully applied for these systems. [26] By introducing more accurate short-range Hartree exchange (from Hartree-Fock calculation method), hybrid exchange-correlation functionals successfully account for physical effects which govern the properties of strongly correlated materials. It introduces, however, either arbitrary, empirical, or semi-empirical parameters (one of which is the ratio of short vs. long range exchange) which severely limits its predictive capability as a first principles method.

Another such solution is a simpler correction term added onto the conventional exchange-correlation functional. While seemingly simple, it has successfully been applied to strongly correlated materials, most notably for transition metal oxides. [27, 28] This correction term stems from another *ab initio* model called the Hubbard model, and as such is referred to as the Hubbard correction. This method is detailed in the next section, and is specific to calculations

of certain localized orbitals within the valence electrons.

2.1.2 Hubbard U correction (DFT+U)

A class of 'strongly correlated' materials such as transition metal oxides (including the most famous example of NiO [29]) are poorly described with regular or classical exchange-correlation functionals such as LDA and GGA. Mott insulators are well-known to exhibit this property, in that LDA or GGA prediction describes them as metals while in reality these materials are insulators. Researchers have known of this problem for some time, and one of the solutions along the years is to adopt the Hubbard correction term U . [28]

The Hubbard correction term U regularly employed in DFT (oft referred to as the DFT+U method) stems from the Hubbard Hamiltonian, a feature of the Hubbard model. [27] As an extension of the tight-binding model, the Hubbard model is used to describe the Mott transition; a transition between metallic and insulating properties due to the Pauli repulsion of localized orbitals. In second quantization form, it is written as follows:

$$\hat{H}_{\text{Hubbard}} = -t \sum_{\langle i,j \rangle, \sigma} (\hat{c}_{i,\sigma}^\dagger \hat{c}_{j,\sigma} + \hat{c}_{j,\sigma}^\dagger \hat{c}_{i,\sigma}) + U \sum_i \hat{n}_{i\uparrow} \hat{n}_{i\downarrow} - \mu \sum_i (\hat{n}_{i\uparrow} + \hat{n}_{i\downarrow}) \quad (2.12)$$

The Hubbard model consists of electron occupation sites in a periodic lattice, where two electrons of opposing spin can occupy one site. The first term describes the 'hopping' of electrons between adjacent sites $\langle i, j \rangle$ with the same spin σ , and is characterized by the hopping term t . The second term, meanwhile, introduces the energy cost U when both spins are occupied, in order to describe the Pauli repulsion. The last term describes occupation of sites from electron chemical potential μ . To describe the changes in occupation, the second quantization notations of $\hat{c}_{i,\sigma}^\dagger$ and $\hat{c}_{i,\sigma}$ are used. Known as the 'creation' and 'destruction' operators, respectively, these operators serve to increase and decrease the occupation of sites in the Hubbard Hamiltonian. The number operator $\hat{n}_{i\sigma}$ results in the occupation number of site i with spin σ , $\hat{n}_{i\sigma} = \hat{c}_{i,\sigma}^\dagger \hat{c}_{i,\sigma}$.

As previously stated, the Pauli repulsion is the source of the Mott transition, and is described by the on-site repulsion U in the Hubbard model (the second term in Equation 2.12). This is the source of the Hubbard U correction, where an energy cost of magnitude U is applied when both spins are occupied. In Mott insulators, this mechanism gains significance and promotes half-filling of the valence band in the ground state, with the cost U raising the conduction band level (realizing an insulating electronic structure). The same holds true for localized $3d$ and $4f$ localized orbitals commonly found in rare earth and several transition metal compounds, for which conventional exchange-correlation functionals unfortunately do not adequately capture this phenomenon.

For DFT, the Hubbard U term is adopted as an artificial correction to the exchange-correlation functional in DFT+U. Within the DFT+U implementation of Anisimov, *et al.* [30], the U correction is added onto the exchange-correlation term as a function of occupation of localized orbitals. Two parameters, U and J , appear within this implementation, respectively controlling for the strength of Coulomb and exchange interactions for localized orbitals, while delocalized orbitals (s and p orbitals) are still well-described by regular DFT.

For conventional exchange correlation functionals LDA and GGA, the Hubbard term effectively provides a solution to the self-interaction problem. Equation 2.5 shows the Hamiltonian form of the Kohn-Sham equation, which consists of the kinetic energy and the potential energy V , the latter consisting of the Hartree term and the exchange correlation term. Strictly speaking,

the potential term V^{ij} represents interaction between electrons with different quantum numbers i and j . Each electron possesses a different orbital and spin (quantum number), and naturally terms representing interactions between electrons of the same orbital *and* spin (self interaction) should be taken out of the equation ($i = j$ terms in Equation 2.13).

$$V^{ij} = \sum_{i \neq j} V_{\text{H}}^{ij} + \sum_{i \neq j} V_{\text{XC}}^{ij} \quad (2.13)$$

However, this self interaction is included in the formulation of the Hartree term, as a representation of Coulomb interaction with a field of electron density $n(\mathbf{r})$ (without distinguishing electron orbital and spin). While it provides a relatively convenient method of integration, the generalized formulation also means that self interaction is included within the Hartree term. Exact exchange correlation functional would cancel out this self interaction present in the Hartree term and provides exact solutions. However, LDA and GGA exchange correlation functionals are constructed as well as a function of $n(\mathbf{r})$, and as such does not provide self interaction cancellation in a rigorous manner.

While LDA and GGA has been shown to be effective enough to cancel out the self interaction for delocalized orbitals, the self interaction error becomes quite significant for localized orbitals. The Hubbard correction effectively serves as the penalty term to rectify this imbalance, specifically treating localized orbitals where this error becomes significant. The Hubbard parameters U and J , in turn, can be considered as the strength of this penalty term.

Original formulation

The original implementation of DFT+U [28–31] adds two correction terms to the exchange-correlation functional:

$$E[n(\mathbf{r})] = E_{\text{DFT}}[n(\mathbf{r})] + E_{\text{Hub}}[n_m^{I\sigma}] - E_{\text{DC}}[n^{I\sigma}] \quad (2.14)$$

As previously stated, s and p delocalized states are well described by DFT: therefore, $n^{I\sigma}$ and $n_m^{I\sigma}$ (atom I , spin σ , and magnetic moment index m) refer to the density of electrons in localized orbitals only, which are usually $3d$ orbitals in transition metals and $4f$ orbitals in rare earth compounds. These orbitals are commonly referred to as ‘‘Hubbard sites’’, and the second and third terms in Equation 2.14 are exclusively applied to these orbitals as part of the DFT+U scheme. The second term accounts for the interactions in localized orbitals, which is calculated using the Hubbard scheme. The third term is known as the ‘‘double counting’’ term, which aims to subtract the energy of localized orbitals from the first (regular DFT) term, as the addition of the first and second terms mean that the energy contribution from Hubbard sites are counted twice (once as a delocalized/regular DFT scheme in the first term, and once again in the second term as a Hubbard scheme). The double counting term subtracts the contribution of Hubbard sites calculated as a regular DFT scheme, as a function of electron density of a certain atom I and spin σ ($n^{I\sigma} = \sum_m n_m^{I\sigma}$).

The original implementation of DFT+U by Anisimov *et al.* is well-suited for the linear muffin-tin orbital (LMTO) basis set, but is not generalized to include other forms of basis sets. Needless to say, it is also ill-suited for the plane-wave basis set used in this work. Instead, the Dudarev [24] scheme is used in this work, which is (most importantly) basis set independent, also incorporating the generalized basis set for LDA+U by Liechtenstein *et al.* [32] For plane-waves basis sets, eigenstates of Hubbard sites are projected onto localized basis sets and are

then treated with Hubbard correction. The occupation matrix elements $n_{mm'}^{I\sigma}$ are defined as:

$$n_{mm'}^{I\sigma} = \sum_{\mathbf{k}, \nu} f_{\mathbf{k}, \nu}^{\sigma} \langle \psi_{\mathbf{k}, \nu}^{\sigma} | P_{mm'}^I | \psi_{\mathbf{k}, \nu}^{\sigma} \rangle \quad (2.15)$$

where the eigenstates $\psi_{\mathbf{k}, \nu}^{\sigma}$ corresponding to crystal momentum \mathbf{k} , band ν , spin σ , and occupation $f_{\mathbf{k}, \nu}^{\sigma}$ are projected onto pseudo-atomic (localized) wavefunctions by the generalized projector $P_{mm'}^I$:

$$P_{mm'}^I = |\varphi_m^I\rangle \langle \varphi_{m'}^I| \quad (2.16)$$

and for $P^I = \sum_m P_{mm}^I$, the total occupation of localized orbitals for atom I ,

$$n^I = \sum_{\sigma} \sum_{\mathbf{k}, \nu} f_{\mathbf{k}, \nu}^{\sigma} \langle \psi_{\mathbf{k}, \nu}^{\sigma} | P^I | \psi_{\mathbf{k}, \nu}^{\sigma} \rangle = \sum_{\sigma, m} n_{mm}^{I\sigma} \quad (2.17)$$

Lichtenstein's formulation for the Hubbard correction term E_{Hub} (Equation 2.14) is derived from screened Coulomb interactions V_{ee} between Hubbard sites, expressed in Hartree-Fock method terms:

$$E_{\text{Hub}} [\{n_{mm'}^I\}] = \frac{1}{2} \sum_{\{m\}, \sigma} \left\{ \langle m, m'' | V_{ee} | m', m''' \rangle n_{mm'}^{\sigma} n_{m''m'''}^{-\sigma} \right. \\ \left. + (\langle m, m'' | V_{ee} | m', m''' \rangle - \langle m, m'' | V_{ee} | m''', m' \rangle) n_{mm'}^{\sigma} n_{m''m'''}^{\sigma} \right\} \quad (2.18)$$

with the notation in Equation 2.18 defined as:

$$\langle m, m'' | V_{ee} | m', m''' \rangle = \int \int \psi_{lm}^*(\mathbf{r}) \psi_{lm'}^*(\mathbf{r}) \frac{e^2}{|\mathbf{r} - \mathbf{r}'|} \psi_{lm'}(\mathbf{r}') \psi_{lm'''}(\mathbf{r}') d\mathbf{r} d\mathbf{r}' \quad (2.19)$$

The double counting term E_{DC} is defined as:

$$E_{\text{DC}} [\{n^I\}] = \sum_I \frac{U}{2} n^I (n^I - 1) - \sum_I \frac{J}{2} [n^{I\uparrow} (n^{I\uparrow} - 1) + n^{I\downarrow} (n^{I\downarrow} - 1)] \quad (2.20)$$

Parameters U and J describe the screened Coulomb and exchange interactions, respectively. The values of U and J were calculated by Anisimov *et al.* by perturbation of a constrained occupation matrix element $n_{mm'}^{I\sigma}$, following the preceding work of Gunnarsson *et al.* [33] with LMTO basis set. Cococcioni *et al.* [1] would go on to develop a similar method for use with the plane-wave basis set, implemented in the QUANTUM ESPRESSO code. [34]

Determination of Hubbard U

This work adopts the DFT+U implementation of Cococcioni and de Gironcoli [1], which makes use of the effective Hubbard parameter $U_{\text{eff}} = U - J$ instead, greatly simplifying the earlier scheme of Anisimov *et al.* By effectively ignoring the exchange parameter J , this approximation allows the calculation of the U_{eff} parameter from first-principles, which is quite useful in the case where few empirical data of the target material is available. By constraining the occupation of a Hubbard site and introducing perturbations, the relaxation stemming from the perturbation

can be used to compute the U_{eff} parameter. The simplified energy functional, with $J = 0$, is as follows:

$$\begin{aligned}
E[n(\mathbf{r})] &= E_{\text{DFT}}[n(\mathbf{r})] + E_{\text{Hub}} \left[\{n_{mm'}^I\} \right] - E_{\text{DC}} \left[\{n^I\} \right] \\
&= E_{\text{DFT}}[n(\mathbf{r})] + \frac{U_{\text{eff}}}{2} \sum_I \sum_{m,\sigma} \left\{ n_{mm}^{I\sigma} - \sum_{m'} n_{mm'}^{I\sigma} n_{m'm}^{I\sigma} \right\} \\
&= E_{\text{DFT}}[n(\mathbf{r})] + \frac{U_{\text{eff}}}{2} \sum_{I,\sigma} \text{Tr} \left[\mathbf{n}^{I\sigma} (1 - \mathbf{n}^{I\sigma}) \right]
\end{aligned} \tag{2.21}$$

it is clear that the combined E_{Hub} and E_{DC} can be calculated by diagonalizing the occupation matrix for localized orbitals:

$$\mathbf{n}^{I\sigma} \mathbf{v}_i^{I\sigma} = \lambda_i^{I\sigma} \mathbf{v}_i^{I\sigma} \tag{2.22}$$

with orbital occupation as eigenvalues $0 \leq \lambda_i^{I\sigma} \leq 1$. The energy functional becomes:

$$E[n(\mathbf{r})] = E_{\text{DFT}}[n(\mathbf{r})] + \frac{U_{\text{eff}}}{2} \sum_{I,\sigma} \sum_i \left[\lambda_i^{I\sigma} (1 - \lambda_i^{I\sigma}) \right] \tag{2.23}$$

As such, the U_{eff} correction raises the total energy for fractional occupation ($0 < \lambda_i^{I\sigma} < 1$), and reduces to the regular DFT functional for integer values of occupation. This is connected to the physical meaning of the Hubbard U correction within this scheme, discussed later on.

The aforementioned correction favoring integer occupation of localized orbitals is determined in magnitude by the value of parameter U_{eff} . Following the original implementation of DFT+ U by Anisimov *et al.* [30], the value of U_{eff} is obtained by a perturbation scheme with constrained occupation of the Hubbard site. A slight difference is present due to the difference in basis sets used: Anisimov's method uses LMTO representation and decouples completely the localized orbitals from the delocalized ones. By utilizing the same plane-wave basis set for all orbitals, the method of Cococcioni and de Gironcoli needs to separate the nonlinear change in energy due to rehybridization of orbitals upon relaxation of the occupation-constrained localized orbitals. This change in energy is unrelated to the Hubbard U_{eff} (on-site Coulomb repulsion) and must be subtracted from the total change in energy due to perturbation.

Lagrange multiplier α_I is applied to constrain the localized orbital occupation n_I , to construct an expression for the total energy functional as a function of this occupation:

$$E[\{q_I\}] = \min_{n(\mathbf{r}), \alpha_I} \left\{ E[n(\mathbf{r})] + \sum_I \alpha_I (n_I - q_I) \right\} \tag{2.24}$$

The correction parameter U_{eff} is contained within the curvature (second derivative) of $E[\{q_I\}]$ with respect to the constraint q_I . This corresponds to the energy cost of constraining integer occupations in Hubbard sites. The previously mentioned change in energy due to rehybridization is obtained from the equivalent curvature of energy with respect to occupation constraint, but within the Kohn-Sham non-interacting scheme:

$$E^{KS}[\{q_I\}] = \min_{n(\mathbf{r}), \alpha_I^{KS}} \left\{ E^{KS}[n(\mathbf{r})] + \sum_I \alpha_I^{KS} (n_I - q_I) \right\} \tag{2.25}$$

As such, the U_{eff} parameter is obtained from the subtracted curvature of Equations 2.24 and 2.25,

$$U = \frac{\partial^2 E[\{q_I\}]}{\partial q_I^2} - \frac{\partial^2 E^{KS}[\{q_I\}]}{\partial q_I^2} \quad (2.26)$$

Application of Janak theorem [35] turns the second derivatives of Equation 2.26 into first derivatives of the eigenvalue, or α_I in this case (according to Dederichs *et al.* [36]):

$$\frac{\partial E[\{q_I\}]}{\partial q_I} = -\alpha_I, \quad \frac{\partial E^{KS}[\{q_I\}]}{\partial q_I} = -\alpha_I^{KS} \quad (2.27)$$

transforming the second derivatives in Equation 2.26 into

$$\frac{\partial^2 E[\{q_I\}]}{\partial q_I^2} = -\frac{\partial \alpha_I}{\partial q_I}, \quad \frac{\partial^2 E^{KS}[\{q_I\}]}{\partial q_I^2} = -\frac{\partial \alpha_I^{KS}}{\partial q_I} \quad (2.28)$$

Practically speaking, in calculations it is much more useful to set the Lagrange multipliers α_I as the independent variables, which is achievable through a Legendre transform:

$$\begin{aligned} E[\{\alpha_I\}] &= \min_{n(\mathbf{r})} \left\{ E[n(\mathbf{r})] \sum_I \alpha_I n_I \right\} \\ E^{KS}[\{\alpha_I^{KS}\}] &= \min_{n(\mathbf{r})} \left\{ E^{KS}[n(\mathbf{r})] \sum_I \alpha_I^{KS} n_I \right\} \end{aligned} \quad (2.29)$$

with density response functions χ_{IJ} and χ_{IJ}^0 defined as

$$\begin{aligned} \chi_{IJ} &= \frac{\partial^2 E}{\partial \alpha_I \partial \alpha_J} = \frac{\partial n_I}{\partial \alpha_J} \\ \chi_{IJ}^0 &= \frac{\partial^2 E^{KS}}{\partial \alpha_I^{KS} \partial \alpha_J^{KS}} = \frac{\partial n_I}{\partial \alpha_J^{KS}} \end{aligned} \quad (2.30)$$

to represent the first-level derivative of energy in Hubbard site I with respect to perturbation in site J . Combining Equations 2.26, 2.28, and 2.30, the calculation of U_{eff} is obtained:

$$U = -\frac{\partial \alpha_I}{\partial q_I} - \left(-\frac{\partial \alpha_I^{KS}}{\partial q_I} \right) = -\frac{1}{\chi_{II}} - \left(-\frac{1}{\chi_{II}^0} \right) \quad (2.31)$$

The linear response functions of perturbation α_I from both interacting and non-interacting (many body and Kohn-Sham) schemes are required in order to calculate U_{eff} . Practically speaking, both can be calculated from the relaxed and unrelaxed Hubbard site occupations n^I from perturbation α_I . The unrelaxed ('bare') occupation represents the non-interacting response, while the relaxed ('converged') occupation represents the response of Hubbard site under screening effects from the other orbitals. Since the first derivatives of the occupation is required, a series of calculations involving various values of α_I is performed, obtaining 'bare' (first iteration) and 'converged' (last iteration) Hubbard site occupations, and finding both linear response functions as slopes of linear regressions:

$$\begin{aligned} n_I [\{\alpha_I\}] &= \chi_{II} \alpha_I + C \\ n_I^{KS} [\{\alpha_I\}] &= \chi_{II}^0 \alpha_I + D \end{aligned} \quad (2.32)$$

The Hubbard U can then be obtained as in Equation 2.31:

$$U = \frac{1}{\chi_{II}^0} - \frac{1}{\chi_{II}} \quad (2.33)$$

for the Hubbard site I .

Example of determination of effective Hubbard U parameter

The following is an example of the scheme for determining U_{eff} for the Hubbard site of NdB_6 . By introducing multiple perturbations in the form of the parameter α , and drawing linear response functions for both the 'bare' and 'converged' series (first and last iterations of the self-consistent calculations), the U_{eff} parameter can be determined. Using small values of perturbation α (-0.08, -0.06, ..., 10^{-40} , 0.02, ..., 0.08), the Hubbard site occupations are plotted and linear fittings are performed using the least-squares method:

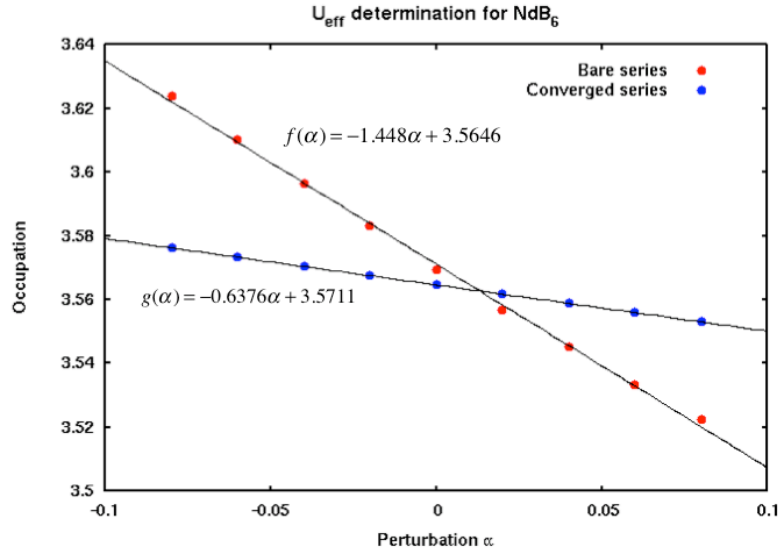


Figure 2.4: Linear regressions of orbital occupation, for the 'bare' and 'converged' series, for NdB_6 Hubbard site

Figure 2.4 shows the 'bare' and 'converged' linear response functions of $f(\alpha) = -1.4480\alpha + 3.5646$ and $g(\alpha) = -0.6376\alpha + 3.5711$, respectively. The parameter U_{eff} value is then computed according to Equation 2.33:

$$U_{\text{eff}} = \frac{1}{-1.4480} - \frac{1}{-0.6376} = 5.3377 \text{ eV} \quad (2.34)$$

Physical meaning of Hubbard U

The physical effect of the U_{eff} correction is to discourage fractional occupation for the Hubbard sites. This is rooted in the physical fact that fractional occupation of a quantum system is im-

possible: it is only possible as a statistical average of systems with different integer occupations. For example, for a non-adiabatic system (possible to exchange electrons with the environment) with the ground state of the system having N electrons, the addition or subtraction of electrons ($N+1$ or $N-1$ electrons) would serve to increase the total energy. Fractional occupations as a statistical mixture of two states are therefore unphysical (unless the two states are somehow degenerate) possibilities for the ground state.

For instance, for a system of $N + \omega$ electrons, with integer N and $0 \leq \omega \leq 1$, the energy:

$$E_{N+\omega} = (1 - \omega) E_N + \omega E_{N+1} \quad (2.35)$$

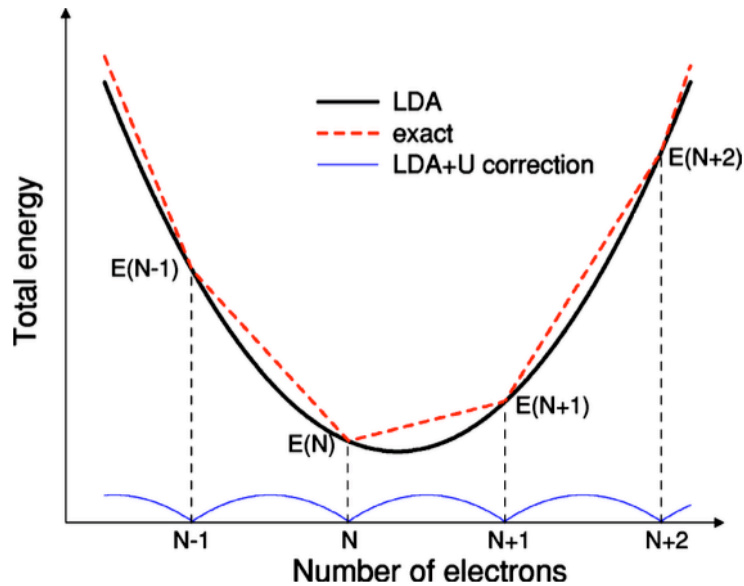


Figure 2.5: Schematic representation of LDA energy profile, the correct (piecewise constant) exact DFT energy profile for fractional occupations, and correction by Hubbard U [1]

This energy profile between integer occupations (piecewise constant) is represented in Figure 2.5 and is not correctly reproduced by LDA or GGA exchange-correlation functionals, which produces continuous energy profile for fractional occupations. The Hubbard U_{eff} is the energy cost to correct this unphysical behavior, which in this diagram would then correctly determine the integer occupation N to be the ground state instead of the unphysical fractional occupation. By rectifying the ground state fractional occupation, the simplified DFT+ U scheme addresses the self-interaction of half-filled localized orbitals which is fundamental to the failure of LDA and GGA for strongly correlated systems.

2.1.3 Forces and phonon calculation

From the self-consistent iteration process of DFT, it is possible to solve the eigenvalue problem in Equation 2.3, obtaining both the eigenvalue E (ground state energy) and eigenfunctions $\psi(\mathbf{r})$ (spatial wavefunction) from the Hamiltonian \hat{H} . The information obtainable from self-consistent iteration, therefore, is not limited to the ground state energy, but also includes all observables obtainable from the spatial wavefunction $\psi(\mathbf{r})$. This includes the atomic forces, as

the first derivative of energy with respect to spatial coordinates \mathbf{r} , which plays a vital role in both optimization of atomic geometry and calculation of atomic vibration (phonon).

The calculation of forces makes use of the Hellmann-Feynman theorem [37], an analytic principle discovered in the 1940s for Hamiltonians which is not exclusive to DFT and also applied in other quantum chemistry methods. The theorem establishes that derivatives of the eigenvalue is obtainable from diagonalization of derivatives of the Hamiltonian:

$$\frac{\delta E}{\delta x} = \left\langle \psi(x) \left| \frac{\delta \hat{H}}{\delta x} \right| \psi(x) \right\rangle \quad (2.36)$$

In the same way, it is possible to calculate the first derivative of forces; that is, the second derivative of energy with respect to spatial coordinates \mathbf{r} . The resultant matrix of second derivatives is referred to as the Hessian matrix and is key in performing optimization of crystal geometry, discussed in the following section.

Geometry optimization

The ground state crystal structure of compounds are first optimized before reliable electronic structure calculations may take place. Within these calculations, apart from ground state energy optimization with respect to electron density (see Section 2.1.1), it must also be optimized with respect to atomic positions in the crystal. The Broyden-Fletcher-Goldfarb-Shanno (BFGS) algorithm is commonly used to optimize the geometry [38], and for phonon calculations it is desirable to optimize the geometry not just with respect to the ground state energy, but also atomic forces as well (setting a maximum allowable value for atomic forces) as will be discussed in harmonic and quasi-harmonic approximations employed in phonon calculations (see Section 2.1.3).

The GGA exchange-correlation functional is known to reliably reproduce atomic lattice constants for transition metals during geometry optimization, while LDA sometimes underestimates lattice constants. There is then motivation to choose GGA over LDA when dealing with transition metal compounds, extrapolating this accuracy toward atomic forces as well. As such, phonon calculations in particular benefit from proper choice of the exchange-correlation functional, largely stemming from the reliability of calculation of forces.

Phonon calculation

Chemical bonds between atoms in a quantum system also dictate how vibration of atomic positions occur. Most importantly, these bonds couple the vibrations of one atom with others in its chemical environment. In short, in a molecule or solid, no single atom vibrates on its own. Classically, chemical bonds between atoms in a quantum system can be viewed as springs with a certain spring constant, influencing how waves propagate within the system. The collective vibrations possess normal modes with discrete levels of energy, referred to as phonons.

As photons are defined as discrete levels of electromagnetic energy, phonons are defined as the discrete levels of *vibrational* energy in a quantum system. Studying phonon properties in materials is vital in understanding how energy propagates through said material. As such, it is important in the study of either thermal and acoustic properties of materials. One of these properties is the specific heat under constant pressure or C_p , which is significant due to its relation with the entropic term in Equation 1.1,

$$\int_{T_1}^{T_2} \frac{C_p(T)}{T} \delta T = S(T_2) - S(T_1) \quad (2.37)$$

CALPHAD is able to use Equation 2.37 to fit parameters in the Gibbs model relating to the entropy term. Therefore, it is desirable to be able to calculate C_p entirely from first-principles. C_p can be calculated from phonon frequencies (vibrational frequencies of the normal modes of atomic oscillation) using the Quasi-Harmonic Approximation.

The harmonic approximation essentially models vibrations in a quantum system of N -atoms as a combination of $3N$ independent harmonic oscillators, with the amplitude of atomic vibrations assumed to be insignificantly small compared to the interatomic distances. By imposing this limitation and expanding the Taylor expansion of atomic oscillation to the second-order, phonon frequencies may be obtained as solutions to the equation of motion. These frequencies depend on the wavevector of the first Brillouin zone (\mathbf{q} -vectors), in the reciprocal space.

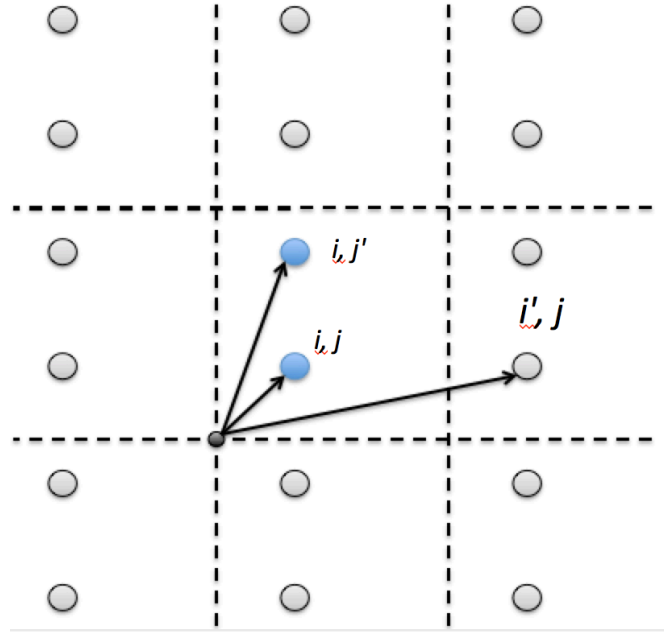


Figure 2.6: Schematic representation of periodic simulation cells with indices i and atomic positions j

Figure 2.6 shows the representation of periodic boundary conditions for solids and the indices of i and j which respectively refers to images of periodic cells and atomic sites in a unit cell. The vibrational potential ϕ is expanded in a Taylor series to the second order:

$$\phi = \phi_0 + \sum_{ij,\alpha} \left(\frac{\partial \phi}{\partial r_\alpha(ij)} \right)_0 \Delta r_\alpha(ij) + \sum_{ij,\alpha} \sum_{i'j',\beta} \left(\frac{\partial^2 \phi}{\partial r_\alpha(ij) \partial r_\beta(i'j')} \right)_0 \Delta r_\alpha(ij) \Delta r_\beta(i'j') + \dots \quad (2.38)$$

with Cartesian axes x- y- and z-axes represented by indices α and β . ϕ_0 is a constant term which can be taken as zero or base potential. The first derivative of ϕ , meanwhile, is the atomic force on directions α and β . With the assumption that the atomic structure is optimized to the equilibrium state, the resultant force on any atom (ij) is also zero. The second derivative of ϕ is then the main focus of the harmonic approximation, also known as the force constants Φ :

$$\Phi_{\alpha\beta}(ij, i'j') = \frac{\partial^2 \phi}{\partial r_\alpha(ij) \partial r_\beta(i'j')} = \frac{\partial F_\alpha(ij)}{\partial r_\beta(i'j')} \quad (2.39)$$

With the frozen phonon approximation, Φ is calculated using finite displacement of atoms from their equilibrium sites in the lattice:

$$\Phi_{\alpha\beta}(ij, i'j') = -\frac{F_\beta(i'j'; \Delta r_\alpha(ij)) - F_\beta(i'j')}{\Delta r_\alpha(ij)} \quad (2.40)$$

For each displacement and atomic force component forming the force constant matrix as defined:

$$\Phi(ij, i'j') = \begin{bmatrix} \Phi_{xx} & \Phi_{xy} & \Phi_{xz} \\ \Phi_{yx} & \Phi_{yy} & \Phi_{yz} \\ \Phi_{zx} & \Phi_{zy} & \Phi_{zz} \end{bmatrix} \quad (2.41)$$

In order to switch to a reciprocal space representation, a Fourier transform is performed on the force constants matrix.

$$D_{\alpha\beta}(jj', \mathbf{q}) = \frac{1}{\sqrt{m_j m_{j'}}} \sum_{i'} \Phi_{\alpha\beta}(0j, i'j') \exp[\mathbf{iq} \cdot (\mathbf{r}_{i'j'} - \mathbf{r}_{0j})] \quad (2.42)$$

with m_j the effective mass of atom in position j , and $i = 0$ referring to the original unit cell. The dynamical matrix $D(jj', \mathbf{q})$ is then formed:

$$D(jj', \mathbf{q}) = \begin{bmatrix} D_{xx} & D_{xy} & D_{xz} \\ D_{yx} & D_{yy} & D_{yz} \\ D_{zx} & D_{zy} & D_{zz} \end{bmatrix} \quad (2.43)$$

Phonon frequencies $\omega(\mathbf{qv})$ can be obtained by solving for the eigenvalue problem in Equation 2.44. The eigenvalue problem is as defined:

$$\sum_{j', \beta} D_{\alpha\beta}(jj', \mathbf{q}) \epsilon_\beta(j', \mathbf{qv}) = [\omega(\mathbf{qv})]^2 \epsilon_\alpha(j, \mathbf{qv}) \quad (2.44)$$

where the eigenfunctions are the polarization vectors $\epsilon_\alpha(j, \mathbf{qv})$ for an N -atom system, a $3N$ -component eigenvector containing the normal modes of vibration. By diagonalization of the dynamical matrix, phonon frequencies ω may be obtained:

$$\sum_{j', \alpha\beta} \epsilon_\alpha^*(j, \mathbf{qv}) D_{\alpha\beta}(jj', \mathbf{q}) \epsilon_\beta(j', \mathbf{qv}') = [\omega(\mathbf{qv})]^2 \delta_{vv'} \quad (2.45)$$

Phonon frequencies may be utilized to calculate the specific heat under constant volume or C_v .

$$C_v = \sum_{\mathbf{qv}} k_B \left(\frac{\hbar \omega(\mathbf{qv})}{k_B T} \right)^2 \frac{\exp\left(\frac{\hbar \omega(\mathbf{qv})}{k_B T}\right)}{\left[\exp\left(\frac{\hbar \omega(\mathbf{qv})}{k_B T}\right) - 1 \right]^2} \quad (2.46)$$

However, the harmonic approximation is not enough to obtain the specific heat in constant

pressure or C_p as previously stated. The Quasi-Harmonic approximation (QHA) is required to introduce volume dependence. The relation of C_v and C_p is a term introducing volume dependence,

$$C_p(V, T) = C_v + TVB_0\alpha^2(T) \quad (2.47)$$

where B_0 is the bulk modulus and $\alpha(T)$ the thermal expansion coefficient from the ground state volume V_0 , defined as:

$$\alpha(T) = \frac{1}{V_0} \left(\frac{\partial V}{\partial T} \right)_P \quad (2.48)$$

The open-source phonopy [39] Python package is used in this work to calculate phonon frequencies and C_p with the VASP plane-wave DFT code [40–43] used as force calculators (to calculate atomic forces and form the force constant matrix $\Phi(ij, i'j')$). Initial geometry optimization (that reduces the first derivative of ϕ to zero in Equation 2.38) is also performed with the VASP package. The phonopy software package parses the crystal structure information within VASP input files and can utilize crystal symmetry to minimize the number of atomic finite displacements which need to be calculated to form the complete force constant matrix. After finite displacement calculations are complete, routines within the phonopy code calculate the dynamical matrix and the phonon frequencies as well.

QHA in phonon calculations is implemented by repeating the phonon calculations in one unit cell volume and applying it to other unit cells in which the volume has been slightly increased and decreased. In this work, the increment unit cell volumes from -5%, -4%, ..., -1%, 0% (ground state), 1%, ..., 5% is used for the QHA. An energy-volume ($E - V$) parabolic curve is obtained and fitted to the third order Birch-Murnaghan equation of state [44], shown in Equation 2.49:

$$E(V) = E_0 + \frac{9V_0B_0}{16} \left\{ \left[\left(\frac{V_0}{V} \right)^{\frac{2}{3}} - 1 \right]^3 B'_0 + \left[\left(\frac{V_0}{V} \right)^{\frac{2}{3}} - 1 \right]^2 \left[6 - 4 \left(\frac{V_0}{V} \right)^{\frac{2}{3}} \right] \right\} \quad (2.49)$$

The results of this fitting include the optimized unit cell volume V_0 and bulk modulus B_0 . It also leads to the volume thermal expansion $\alpha(T)$ as defined in Equation 2.48. Needless to say, these quantities eventually lead to the calculation of C_p .

The entire workflow of the phonon calculations in this work is reflected in the schematic of Figure 2.7.

Lattice vibrations contribute the single most significant factor to the total C_p , although there are other factors at play as well. For example, a shift in magnetic ordering (usually at low T) often introduces a peak in C_p due to the heat required for the magnetic ordering change. This results in a magnetic ordering contribution C_{mag} which results in this peak.

Another factor is that of the electronic contribution C_{elec} stemming from excitation of electrons occupying half-filled bands at the Fermi level for metallic systems. While inconsequential at low T , the electronic contribution is more significant at high T , and since CALPHAD modeling usually reaches $T < 3000$ K, it is important to include C_{elec} for metallic systems. Accounting for the electronic contribution, fortunately, does not require much computational cost, as it can be derived from density of states (DOS) at the Fermi level ($D(E_F)$) for metallic systems:

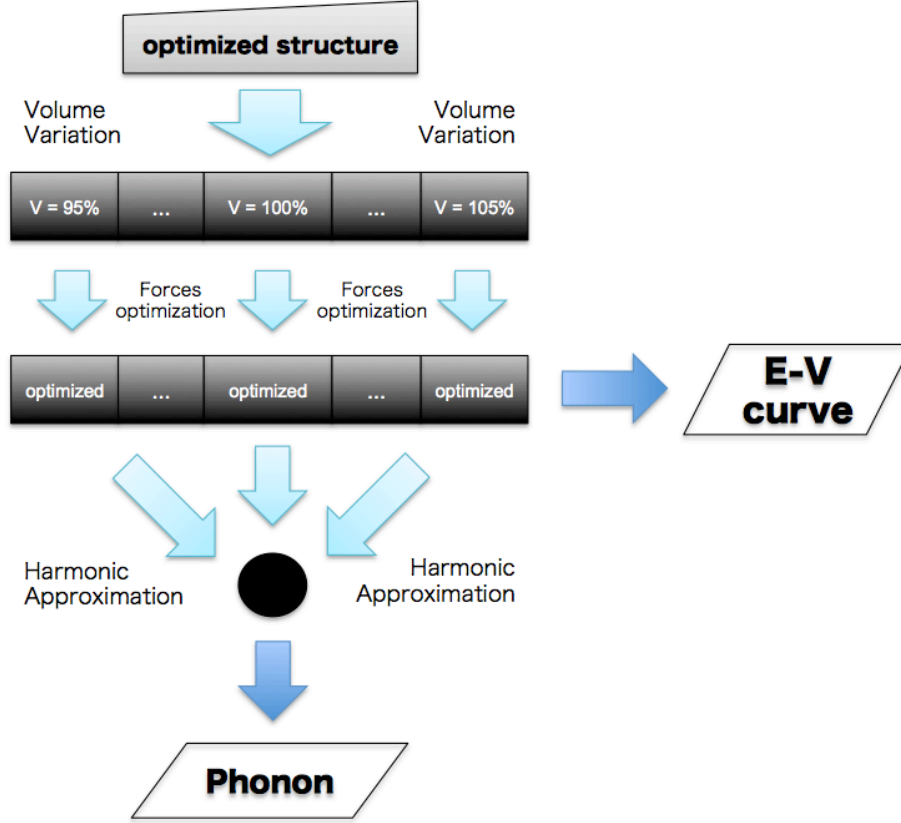


Figure 2.7: Schematic workflow of phonon calculations in this work

$$C_{\text{elec}}(T) = \frac{\pi^2}{3} k_B^2 T D(E_F) \quad (2.50)$$

which is an approximation from the free electron case. The density of states can be computed easily from self-consistent calculations.

2.2 CALPHAD

Based on the concept of “lattice stability” by Kaufman [45], the CALPHAD method has grown into one of the most important tools for researchers and engineers in materials science. By modeling the Gibbs energy of competing phases, it is then possible to predict when phase transitions from one to the other occur, as a function of temperature T , pressure P , or composition. Merging phase diagram with the field of thermodynamics, CALPHAD enables the computational construction of phase diagrams, greatly reducing the effort it takes to draw one in the first place.

The basic concept is that of the minimization of the Gibbs energy. Gibbs energy models are formed for the competing phases, and by way of minimization, CALPHAD users can predict which phase is at the lowest in Gibbs energy, and establish it as the stable phase at a certain point in the phase diagram. The total Gibbs energy may even be formed from fractions of the Gibbs energy of phases, possibly leading to global minima where two or more phases may exist

simultaneously as the most stable configuration, per Gibbs' phase rule:

$$f = c + 2 - p \quad (2.51)$$

f denotes the number of degrees of freedom, c represents the number of components, and p is the number of phases which exist simultaneously. '2' represents the variables T and P , and it is reduced for an isothermal or isobaric configuration. For a T v P phase diagram of water, for example, $c = 1$ for water, resulting in $f = 3 - p$ as the Gibbs phase rule. The maximum number of phases that can exist simultaneously is 3 for a triple point where the degree of freedom $f = 0$, that is, an invariant equilibrium (changing either T or P ruins the equilibrium, leading to a different phase). The same is true for a binary system in an isobaric phase diagram where $c = 2$ but the '2' in the formula is reduced to '1', again leading to a phase rule of $f = 3 - p$ and a maximum of 3 phases existing simultaneously in an invariant equilibrium. Where 2 phases exist simultaneously, $f = 1$ which means that only one degree of freedom may be moved *independently*; in a binary isobaric phase diagram, it is a line (inclined lines mean one of the degrees of freedom is changed *as a function* of the other degree of freedom). These lines represent regions of monovariant equilibria (one degree of freedom). Single-phase regions (including solid solutions) can have $f = 2$ independent degrees of freedom, in this case, of T and x_i (composition). The isobaric case is adopted from this point on (at 1 bar or standard pressure).

The CALPHAD method can be roughly separated into three steps: construction of the Gibbs energy models, the optimization of parameters, and the calculation of the phase diagram, as represented in Figure 1.1. The construction of these Gibbs energy models involve an established practice of working formalisms for binary, ternary, quaternary, *etc.* systems and a measure of optimization based on theoretical and empirical data as well. The software package Thermo-Calc [46] is used to perform the CALPHAD method in this work. Multiple aspects or modules within Thermo-Calc handle different aspects of the CALPHAD framework, as explained below.

2.2.1 Gibbs energy modeling

The GES (Gibbs Energy System) module in Thermo-Calc serves to build the Gibbs energy models based on specifications from the user. Contributions to the Gibbs energy can be roughly separated between the "surface of reference" (srf) and "excess" contributions, from the unreacted reference states and from the interactions between components, respectively. The "excess" Gibbs energy is typically expanded in a power series of T as one of the degrees of freedom. For a temperature-dependent model, the molar Gibbs energy model is expanded in the form of Equation 2.52.

$$G_m^\theta - \sum_i b_i H_i^{\text{SER}} = a_0 + a_1 T + a_2 T \ln(T) + a_3 T^2 + a_4 T^{-1} + a_5 T^3 + \dots \quad (2.52)$$

with H_i^{SER} the enthalpy contributions of unary reference states, and b_i the stoichiometric fraction of element i for phase θ . 'SER' refers to the standard condition at $T = 298.15$ K and $P = 1$ bar, and these unary references are extracted from a database from the Scientific Group Thermodata Europe (SGTE) database referred to as PURE5. [47] This expression is useful in a finite temperature range above the Debye temperature. [5]

In practice, the Redlich-Kister (R-K) polynomial is often used for modeling of excess contribution from interaction in binary and ternary systems. [48] For a binary system with com-

ponents i and j , the excess term is modeled using the difference between the fractions of i and j :

$$L_{ij} = \sum_{v=0}^k (x_i - x_j)^v \cdot {}^vL_{ij} \quad (2.53)$$

with the powers of v decreasing in significance from 0, 1, .. and the coefficients ${}^vL_{ij}$ usually only described up to the linear order expansion:

$${}^vL_{ij} = {}^va_{ij} + {}^vb_{ij}T \quad (2.54)$$

with the $T \ln(T)$ term being rarely required to model most binary systems. [5] The R-K polynomial coefficients are treated as variables or parameters which will be optimized according to thermodynamic data of constituent phases in the system.

Gibbs energy models are constructed for each phase θ in a binary system, for each of which a set of R-K coefficients are optimized in the subsequent step. Needless to say, the choice of models and number of parameters greatly affect the result of the CALPHAD method. As such, reassessments of phase diagrams involve not only new thermodynamic information, but possibly the application of new models and parameters leading to a more accurate end result as well.

2.2.2 Parameter fitting

The R-K coefficients set in place for phases θ in a binary system are optimized according to thermodynamic information on hand for a set of constituent phases. The optimization or fitting process is handled by the PARROT module in Thermo-Calc. [46] By seeking the minimum in the sum-of-squares of errors (using weights), the fitting process may be performed with an arbitrary number of iterations as needed, as long as suitable initial parameters are used.

Practically, thermodynamic data of constituent phases are collated into a single file before optimization. R-K coefficients are then optimized for one or two phases at a time, in order to efficiently find the global minimum. By adjusting the weights of data so that only relevant thermodynamic information or phase equilibrium are used for an optimization, the R-K coefficients are optimized serially.

Once a series of R-K coefficients have been optimized, the next set may be optimized by including the previous set or even by freezing the previous set so that the optimization process runs more smoothly. Parameter fitting is possibly the most demanding phase of the CALPHAD workflow, as conflicting thermodynamic data might also appear, leading to a large sum-of-squared error value in the optimization. There is no one set path towards efficient optimization, and experience plays a key role for this step.

When the optimization is successful, the complete Gibbs energy models for phases in the system is obtained, and the CALPHAD workflow moves onto the final step. The Gibbs energy models can then be used to predict phase transitions from starting equilibria, thereby enabling the construction of the phase diagram, in this case, as a function of two degrees of freedom T and x_i .

2.2.3 Drawing the phase diagram

Calculations of phase equilibria based on the optimized Gibbs energy models are handled by the POLY module in Thermo-Calc. [46] By setting a first equilibrium point in the configuration space of T and x_i , successive iterations are made to establish Gibbs energy minima and predict the most stable phase or configuration of phases. In this sense, it is then possible to plot the points of phase transitions along the phase diagram, in other words, lines of monovariant equilibria (Section 2.2). Once found, these lines of monovariant equilibria can be traced by independently varying one degree of freedom (either T or x_i) until a triple point (invariant equilibrium) is found or the variation finds a boundary condition (minimum or maximum values of T or x_i , after which the iterations begin anew in a different configuration space. This, along with applying generally established rules of thumb, form the core methodology of calculating the phase diagram in CALPHAD.

One such established rule is what is known as the lever rule [5] which can be used to determine the amount of phase in an equilibrium. The total Gibbs energy is formed from a linearly dependent contribution from the phases present in an equilibrium:

$$G = \sum_{\alpha} m^{\alpha} \cdot G_m^{\alpha} \quad (2.55)$$

The lever rule states that the amount of phase m^{α} ; that is, the contribution of the phase to the total Gibbs energy, is equal to the contribution of fraction of the component i in phase α (x_i^{α}) to the total fraction of the component x_i :

$$x_i = \sum_{\alpha} m^{\alpha} \cdot x_i^{\alpha} \quad (2.56)$$

This rule is invaluable in evaluating equilibria between two or more stoichiometric phases, since the fraction of component x_i and fraction of component in phase x_i^{α} is readily known.

The Thermo-Calc module POST is equipped to perform the plotting of the phase diagram itself, with information of phase equilibria obtained in the POLY module.

Chapter 3

Research Objective

3.1 Permanent Magnets

Magnetism as a physical phenomenon has been of great interest to humanity from its discovery. We have discovered extensive uses for magnetism, from navigation, mechanical, and well into the role magnetic materials play currently in the information age. Permanent magnets, too, have been widely used since their discovery, from small, weak permanent magnets (compasses, fridge magnets) to the most powerful permanent magnets employed today in marvelous engineering projects (electric generators, Large Hadron Collider, *etc.*). Needless to say, permanent magnets would still hold important roles in engineering and industry for some time to come as well.

It is widely known that permanent magnetic materials eventually lose magnetic strength at high temperatures. The source of magnetic phenomenon is the imbalance in populations of electrons with opposing spin moments: the bigger the imbalance, the more magnetic moment an atom possesses. Due to well-known concepts within statistical thermodynamics, the population of electrons possessing certain spin moments constantly fluctuate, and this fluctuation increases in intensity in higher temperatures. At a certain transition temperature (known as the Curie temperature or T_C), this fluctuation causes the macrostate population of opposing spin electrons to effectively be balanced (trending toward greater fluctuation or entropy), leading to the loss of magnetic strength observed. This is why ferromagnetic materials transition into paramagnetic materials above the T_C threshold, which in turn imposes a limitation on permanent magnets, without exception.

This physical fact is why high- T_C permanent magnets are highly sought after, and has always been an objective of improvement for existing permanent magnet materials. In order to increase the working temperature of permanent magnets (*e.g.* electric generators, electric motors), one method which is often employed is by atomic substitution from a base permanent magnet material. Alloying and doping are methods commonly used to enhance physical properties of a base material to suit a performance need for devices. The most famous example would be doping in semiconductors for silicon wafers, where the dopant determines whether an n-type or a p-type semiconductor is fabricated.

A well-known example concerning permanent magnets is that of the $\text{Nd}_2\text{Fe}_{14}\text{B}$ ternary phase. Due to its high magnetization (density of magnetic moment) and coercivity (resistance to demagnetization by external magnetic field), the $\text{Nd}_2\text{Fe}_{14}\text{B}$ is used as the base material for the most powerful permanent magnets commercially available today. One example of this method is the alloying of $\text{Nd}_2\text{Fe}_{14}\text{B}$ with cobalt (Co), creating the $\text{Nd}_2\text{Fe}_{14-x}\text{Co}_x\text{B}$ compound, which

possesses higher T_C than the base $\text{Nd}_2\text{Fe}_{14}\text{B}$. [49] However, this increase in T_C is accompanied by a decrease of the coercivity, which is in turn compensated by substituting Dy into Nd sites (increasing coercivity). [7] This example shows the manipulation material properties by atomic substitution and alloying, which is often used in the industrial world.

This method is not always effective, however, as atomic substitution also changes the stability of the phase. Not all substitutions can be realized as the introduction of atoms of different species in a crystal structure also introduces stress and strain (*e.g.* due to mismatch of atomic radii), and often leads to instability in the crystal structure, leading to deformation, vacancies, or even new phases. Material composition is of course one factor, but changes in temperature and pressure can also allow for new phases and defects to form. In order to properly make use of this method, information on *phase stability* is highly valuable, embodied in the phase diagram.

With the phase diagram, researchers and engineers can quickly identify relevant regions of phase stability, types of phase transition, as well as the atomic composition which produces a stable phase at certain temperatures and pressures. Needless to say, phase diagrams are vital in material fabrication, including the application of atomic substitution, as it effectively dictates which substitutions are physically possible. This need resulted in the development of CALPHAD [5] method of computational thermodynamics, which has been widely used to assess information on phase stability and create phase diagrams using related/relevant thermodynamic information of phases. The Nd-Fe-B ternary system which contains the important $\text{Nd}_2\text{Fe}_{14}\text{B}$ base phase of "permanent neodymium magnets" is of course a valuable target system for CALPHAD. To that end, several assessments of the ternary system have been made [2, 3, 50–53] using available experimental data. However, the small number of data available is a drawback of these assessments, and this work aims to provide a more complete dataset using *ab initio* calculations.

3.2 Overview of the Nd-Fe-B system

Rare earth elements consist of atomic numbers $Z = 57$ (La) to $Z = 71$ (Lu), and is characterized by having $4f$ orbitals as the highest energy levels for the valence electrons. This physical property lends them unique qualities compared to lighter elements, especially concerning spin-orbit coupling (for the so-called heavy fermions) and magnetic properties. The latter is especially true when rare-earth elements are present together with lighter transition metals ($3d$ orbitals), with many among these compounds exhibiting high magnetic moments.

These materials constitute the class of rare earth permanent magnet materials, and the search for better permanent magnet materials usually is concentrated with these compounds as its core. For example, prior to the discovery of $\text{Nd}_2\text{Fe}_{14}\text{B}$, the samarium-cobalt magnet (SmCo_5) used to be a leading candidate for the best permanent magnets. The Nd-Fe-B system, as part of the rare-earth transition metal system, is of no exception, and much has been accomplished in investigation into the properties of its constituent phases, chiefly on $\text{Nd}_2\text{Fe}_{14}\text{B}$.

Published works investigating the Nd-Fe-B system so far has exclusively relied on experimental data. [2, 3, 50–53] Due to the relatively sparse availability of said experimental data however, reassessments of the Nd-Fe-B system rarely include "newly discovered" data, and mostly revolves around the different weighting and model choice in constructing the Gibbs energy models integral in CALPHAD. One example is the homogeneity range of the binary NdB_6 phase [54], which is highly weighted in a recent assessment [2], but hardly appeared in a previous assessment. [3] The constituent binary phases in Nd-Fe-B include the Fe-B, Nd-Fe, and

the Nd-B system, and due to the way Gibbs energy models are generally constructed in CALPHAD, it is necessary to first evaluate for these binary systems as a stepping stone into the goal of the ternary system. As such, it is necessary to not only look at the end goal of the ternary Nd-Fe-B system, but also for these constituent binary systems as well:

3.2.1 Fe-B system

The binary Fe-B system is, in contrast with the other two binary constituents, much more well-documented. This is due to great interest for the Fe-B system, owing to its importance for hardened steel composites (TiB₂-reinforced steel compounds [55]). The binary phase diagram is shown in Figure 3.1 (taken from the work of van Ende and Jung [2]), showing multiple phases present in the system, including the liquid phase, iron phases (α -Fe, δ -Fe, and γ -Fe), the α - and β boron phases, and the stoichiometric alloys FeB and Fe₂B.

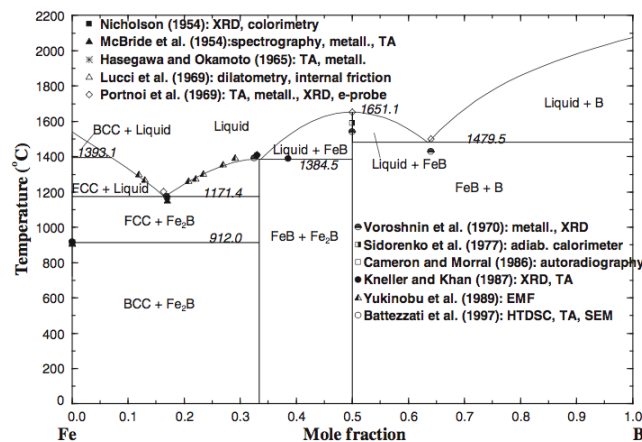


Figure 3.1: Calculated phase diagram of the Fe-B system, thermodynamic assessment by Van Ende and Jung [2]

Between the works dedicated to the Fe-B system, few disagreements exist, including the melting behavior of Fe₂B (peritectic [11] or congruent [2]) and of course of the optimal Gibbs energy model choice within CALPHAD. Works investigating ternary systems containing Fe-B also exist, such as the ternary Fe-Si-B system [56], the model for which necessarily includes a glass transition for the metastable Fe₃B phase. However, it is relatively well-investigated and documented due to reasons previously stated, and as such is beyond the scope of this work, as *ab initio* predictions likely would not provide significant impact.

3.2.2 Nd-Fe system

The Nd-Fe binary system consists of two stable compounds: the Nd₂Fe₁₇ phase and the much more recently discovered Nd₅Fe₁₇. [57, 58] This results in the neglect of the Nd₅Fe₁₇ binary for earlier assessments, such as for the work of Zhang *et al.* [59] While possessing interesting structural and magnetic properties, the Nd-Fe binary system is rarely utilized, with interest on this system chiefly due to the discovery of neodymium permanent magnets in the 1980s and the search for new permanent magnet materials.

Figure 3.2, taken from the work of van Ende and Jung [2], shows the stable phases for the Nd-Fe binary system. These include the liquid phase, the three phases of Fe and two phases

of Nd, and the two aforementioned stable compounds $\text{Nd}_2\text{Fe}_{17}$ and $\text{Nd}_5\text{Fe}_{17}$. The specific heat in constant pressure of $\text{Nd}_2\text{Fe}_{17}$ was measured by Aune and Seetharaman. [60] Unfortunately however, not enough information was listed to reliably convert the units of measurement into SI.

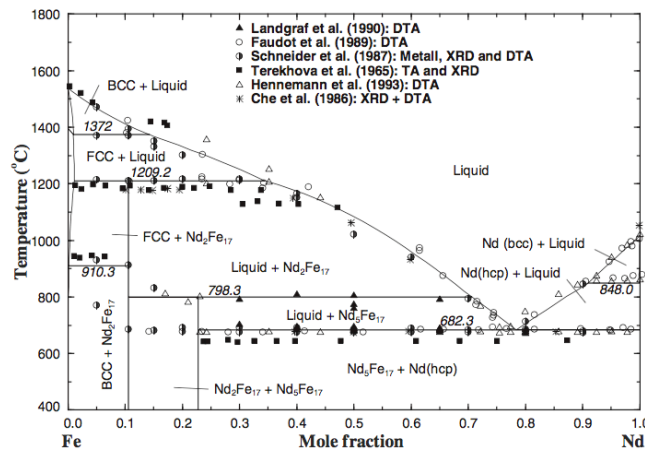


Figure 3.2: Calculated phase diagram of the Nd-Fe system, thermodynamic assessment by Van Ende and Jung [2]

3.2.3 Nd-B system

The binary Nd-B system is in a class of materials important due to their high structural strength at high temperatures, the refractory borides. It possesses the largest number of stable binary compounds out of Fe-B and Nd-Fe, with four available stable compounds NdB_6 , NdB_4 , Nd_2B_5 , and NdB_{66} , in addition of course to the liquid phase and the two phases each for unary B and Nd, as shown in Figure 3.3. [2] Compared to Fe-B (which is well-investigated) and Nd-Fe (too few data) binary systems, Nd-B system is the most ideal system to calibrate the *ab initio* methodology as both impact and validation (by comparison with available data) can be assessed. As briefly mentioned previously, one of these, the NdB_6 binary phase, possesses a homogeneity range toward the B-rich region at higher temperatures. This can be observed in the phase diagram (Figure 3.3 as tie lines towards the B-rich region of NdB_6), which in turn comes from the initial findings of Storms. [54] Direct synthesis calorimetry has provided experimental data on the enthalpy of formation for NdB_4 and Nd_2B_5 [61, 62], and low temperature specific heat information has also been experimentally obtained for some phases. [63,64] NdB_6 by far is the least investigated binary phase in the Nd-B system. However, due to its low symmetry crystal structure, *ab initio* investigation into this particular phase also seems unfeasible (not to mention the disorder inherent in the structure, which would easily multiply the cost of calculation in periodic boundary conditions).

3.2.4 Nd-Fe-B system

As the final goal of the assessment, the ternary Nd-Fe-B system contains the $\text{Nd}_2\text{Fe}_{14}\text{B}$ phase, commonly referred to as the T1 phase. The other two stable phases are likewise referred to as T2 ($\text{Nd}_{1.1}\text{Fe}_4\text{B}_4$) and T3 ($\text{Nd}_5\text{Fe}_2\text{B}_6$). While multiple metastable states exist (such as $\text{Nd}_5\text{Fe}_{18}\text{B}_{18}$ and $\text{Nd}_2\text{Fe}_{23}\text{B}_3$ [2]) these are not always included in the CALPHAD assessment. As might be

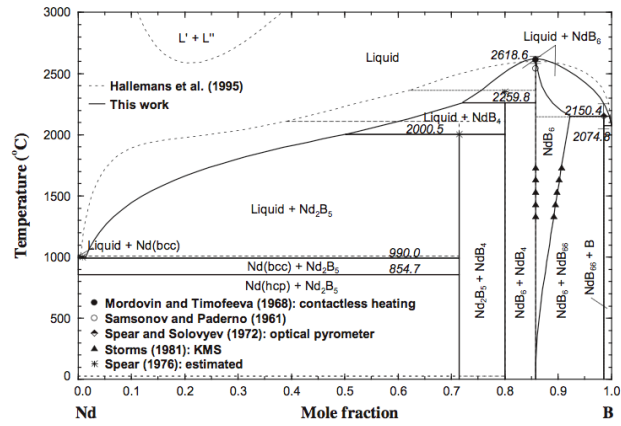


Figure 3.3: Calculated phase diagram of the Nd-B system, thermodynamic assessment by Van Ende and Jung [2]

expected, experimental information is mostly focused on the vital T1 phase, while the other two stable phases do not have much information on them. The isothermal slice (at $T=298$ K) of the Nd-Fe-B is shown in Figure 3.4.

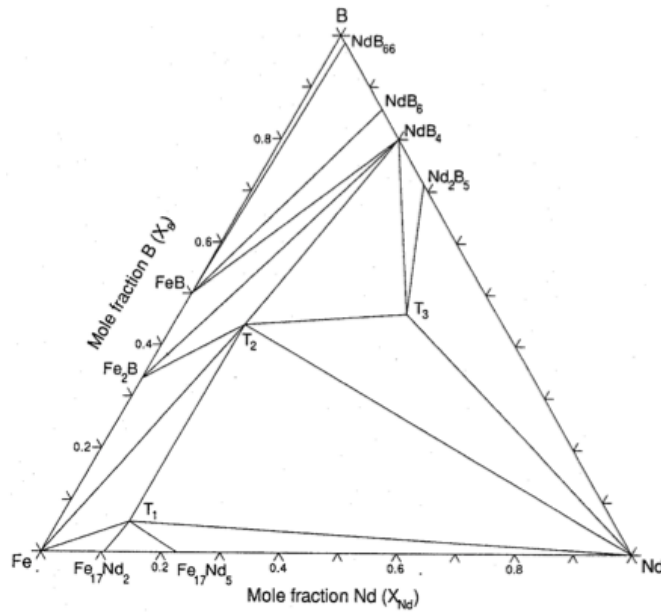


Figure 3.4: An isothermal slice at 25°C of the phase diagram of the Nd-Fe-B system, thermodynamic assessment by Hallems et al [3]

Chapter 4

Results and Discussion

Ab initio investigation into binary and ternary constituent phases of the Nd-Fe-B system is carried out using Quantum ESPRESSO [34], VASP [40–43], and phonopy [39] software packages. Parameter calculations are performed beforehand according to methods outlined in Chapter 2. Afterwards, the BFGS (Broyden-Fletcher-Goldfarb-Shanno) [38] is used to perform geometry optimization, obtaining the relaxed crystal structure used in both the self-consistent field (scf) and phonon calculations. Enthalpy of formation is calculated according to Equation 4.1.

Phonon calculations are performed in order to obtain the specific heat in constant pressure or C_p from 0 K to 3000 K, with increments of 10 K, using the Birch-Murnaghan equation of state (Equation 2.49). The frozen phonon approach is used with volume variations of -5% to +5%, with increments of 1% of the relaxed crystal structure.

4.1 Unary phases

The unary reference states are important in both the enthalpy of formation calculation (Equation 4.1) and the optimization of Gibbs energy models within CALPHAD. The three chosen reference states are the α -Nd (dhcp), α -Fe (bcc), and α -B (rhombohedral) unary phases.

4.1.1 Nd

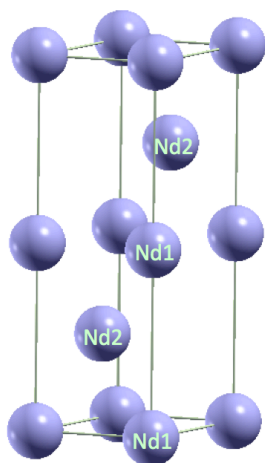


Figure 4.1: Unit cell of ground state Nd

The α -Nd phase is chosen as the reference state, a double hexagonal close-packed (dhcp) crystal structure with space group $P63/mmc$. The experimental work of Nakaue [65] provides the initial crystal structure used (before relaxation). Two Wyckoff positions, Nd1 and Nd2, exist as shown in the Nd simulation unit cell in Figure 4.1. The initial bulk lattice parameters, taken from experimental data, are as follows:

A: 3.6582 Å	α : 90°
B: 3.6582 Å	β : 90°
C: 11.7966 Å	γ : 120°

Initial parameters are only slightly modified in the geometry optimization.

Self-consistent determination of effective Hubbard U correction U_{eff} for the 4f orbitals are conducted, with values of U_{eff} for each Hubbard site:

Nd1: 5.1340 eV

Nd2: 5.2474 eV

The two positions are opposed in spin, leading to an antiferromagnetic ground state consistent with theoretical predictions [66]. Test calculations confirm that the ferromagnetic ordering produces a higher total energy, and therefore, is energetically not favorable compared to the antiferromagnetic ordering, when accounting for the DFT+U method.

4.1.2 Fe

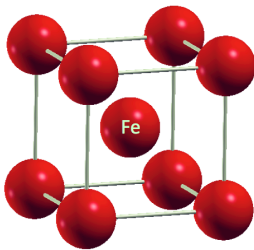


Figure 4.2: Unit cell of ground state Fe

The Fe ground state is the α Fe phase, a body-centered cubic crystal with space group $Im-3m$. The experimental [67] bulk lattice constant of 2.8665 Å is used as the initial structure. The single Hubbard site is determined to have the 3d orbital effective Hubbard U correction of U_{eff} : 3.9182 eV. The ferromagnetic structure of bcc Fe is well-documented to possess magnetic moment of 2.2 μ_B /atom. [68] Our result with the GGA-PBE exchange correlation functional returns a similar magnetic moment value of 2.08 μ_B /atom, while the GGA+U results in a higher magnetic moment of 2.56 μ_B /atom. This is consistent with the results of LDA+U from the work of Fernando *et al.* [69],

which indicates increasing the U parameter would also increase iron site magnetic moment in iron nitrides. It should be noted that the *ab initio* determined value of the U_{eff} correction is significantly higher than the usual value of 1 eV used for iron. The higher magnetic moment obtained suggests the Hubbard U correction in the calculation of iron serves to suppress the occupation of minority spin elements, which is consistent with the meaning of the U_{eff} parameter within this framework, discussed in Section 2.1.2. [1] While not perfectly reproducing the magnetic moment of bulk Fe, the resulting magnetic moment is not necessarily an unphysical value, especially considering the saturation magnetic moment of $\sim 3.5 \mu_B$ /atom. [69]

4.1.3 B

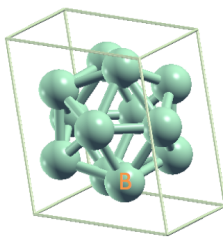


Figure 4.3: Unit cell of α B phase

The ground state of unary boron is the β -B phase, based on the work of Shang *et al.* [70], which found that the α -B phase is energetically less stable by a margin of 3 meV/atom of Helmholtz free energy (F). Another work, meanwhile, found that α -B is energetically more stable. [71] However, the α -B phase is significantly cheaper computationally as it possesses higher symmetry, with the primitive cell containing 12 atoms (compared to the 105 atoms necessary to periodically model the *beta*-B phase). As such, the α -B phase (space group $R-3m$) is chosen as the reference state.

Initial lattice parameters and atomic positions are taken from the experimental work of Will and Kiefer. [72] A primitive cell was con-

structured based on the parameters found in their work:

$$\begin{array}{ll} \text{A: } 5.043 \text{ \AA} & \alpha: 58.096^\circ \\ \text{B: } 5.043 \text{ \AA} & \beta: 58.096^\circ \\ \text{C: } 5.043 \text{ \AA} & \gamma: 58.096^\circ \end{array}$$

Boron is not included as a Hubbard site, due to lack of any $3d$ and/or $4f$ electrons.

4.2 Binary phases

Formation enthalpy calculation results are presented in table form according to the following formula, for a binary A_xB_y phase,

$$E_{\text{form}} = E_{A_xB_y} - xE_A - yE_B \quad (4.1)$$

4.2.1 NdB_6

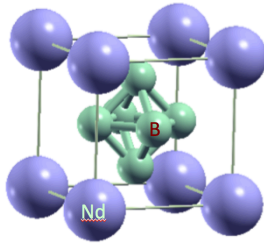


Figure 4.4: Unit cell of NdB_6 phase

Homogeneity range of NdB_6 from the work of Storms [54] is reflected in the two latest phase diagram assessments of the Nd-B binary system: the works of van Ende and Jung [2] and that of Chen. [53] Two simple cubic sublattices of Nd atom and octahedral arrangement of B atoms exist. The work of McCarthy and Tompson [73] provides the initial cubic lattice constant of 4.128 \AA , while the atomic positions are taken from the crystal coordinates (relative to lattice vector lengths) of the prototype structure CaB_6 . [74] U_{eff} parameter is determined to be 5.3377 eV for the single Hubbard site.

Phase	Total Energy [Ry]	Z	x	Calculation
NdB_6	-606.33497819	1	1	-606.33497819
Nd	-2149.34939322	4	1	-537.33734831
B	-137.51514966	12	6	-68.75757483
E_{form} [Ry]				-0.24005506
$E_{\text{form, GGA+U}}$ [kJ/mol.atom]				-45.01888591
Expt. [kJ/mol.atom] [54]				-46.5 ± 1.5
$E_{\text{form, GGA}}$ [kJ/mol.atom]				-51.72035826

Table 4.1: NdB_6 Formation Enthalpy

Table 4.1 shows the enthalpies of formation for NdB_6 obtained by GGA, GGA+U, and from the experimental data of Storms. [54]

The obtained GGA+U result of $-45.019 \text{ kJ/mol.atom}$ is in good agreement with the available experimental data. On the other hand, GGA results in a difference of nearly 7 kJ/mol.atom ($> 5\%$) with experimental results. For CALPHAD's purposes, therefore, the GGA+U formation enthalpy is more reliable than plain GGA as input data.

The specific heat C_p values from $0 < T < 3000 \text{ K}$ is obtained by phonon calculation and are compared to the measurements from the work of Reiffers *et al.* [63], which measured NdB_6

C_p from $T = 4.2$ K to $T = 300$ K within an external magnetic field of various strength. The comparison against a zero external magnetic field is shown in Figure 4.5.

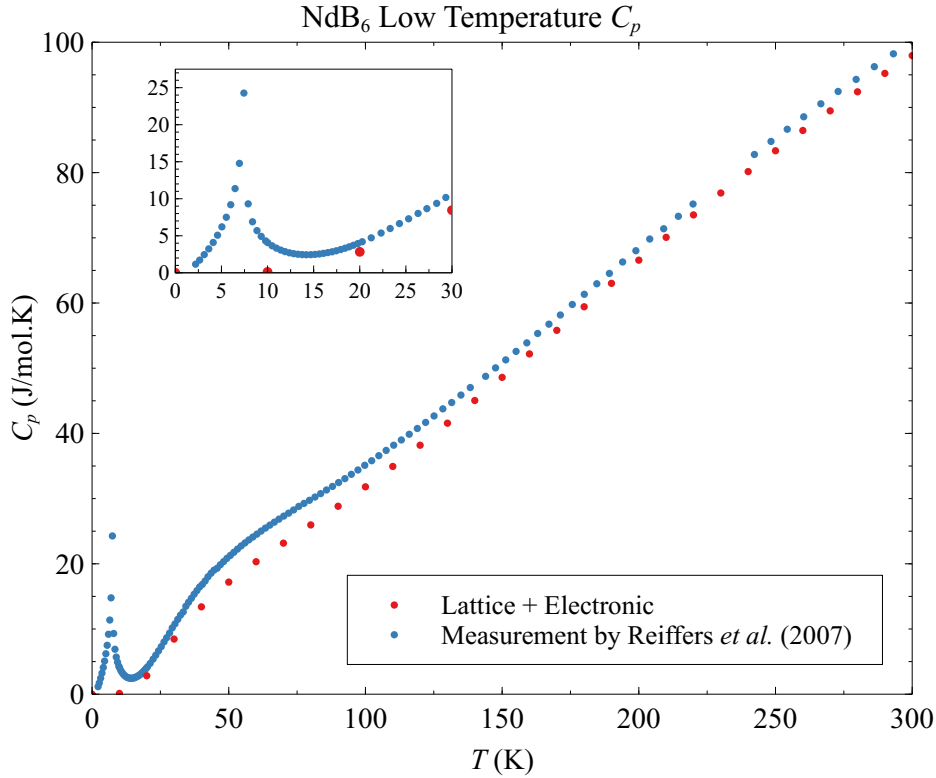


Figure 4.5: C_p from phonon calculation of NdB_6 , in comparison with experimental result

The low temperature spike around $T = 20$ K in the experimental data is caused by the magnetic ordering transition from antiferromagnetic to paramagnetic order. This is not reflected in the *ab initio* results in this work, which takes into account vibrational and electronic contributions only (not from magnetic ordering).

Above $T = 20$ K however, good agreement is reached between this work and the measurement at $T < 300$ K. A room temperature measurement of C_p by Bolgar [4], produces an function of heat capacity from a fitting to the Mayer-Kelly equation, which is deemed valid for the high-temperature range $298.15 \text{ K} < T < 2112 \text{ K}$. The function for for NdB_6 is:

$$C_p(T) = 0.030203T + 117.19 - \frac{3207235}{T^2} \quad (4.2)$$

which translates to the following comparison to phonon calculation results in Figure 4.6. showing a significant difference for $300 < T < 3000$ K, which is the valid temperature range for CALPHAD utilization. In light of the disagreement between the work of Bolgar [4] and the more recent work of Reiffers [63], and the good agreement established in low temperature between the work of Reiffers and this work, we argue that our work will provide a good substitute for the theoretical prediction of Bolgar.

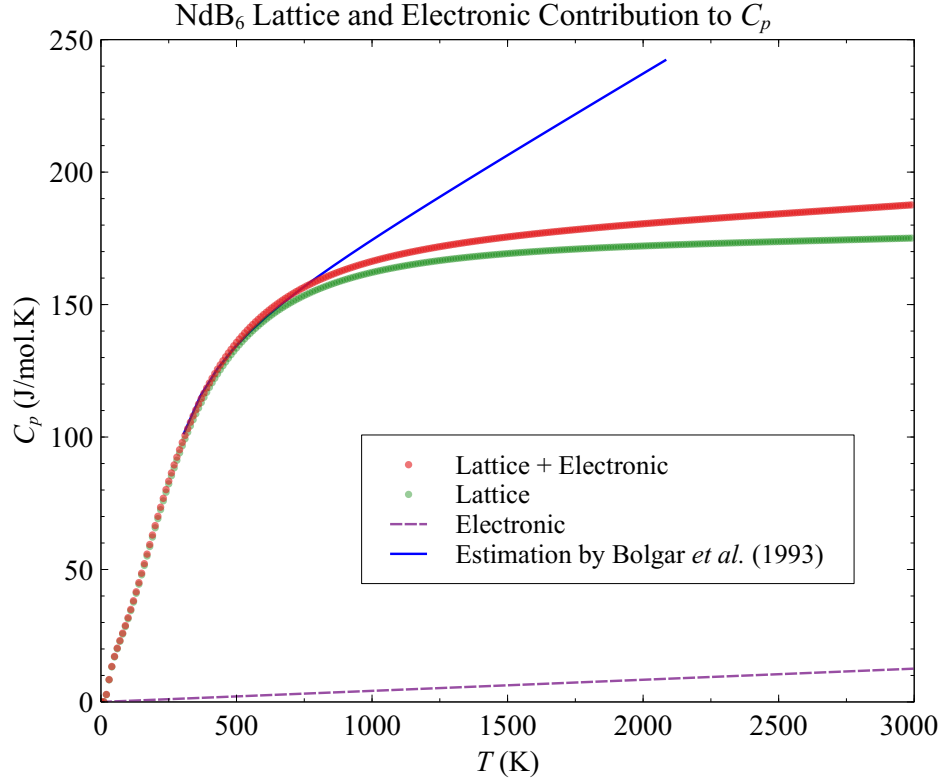


Figure 4.6: C_p from phonon calculation of NdB_6 , in comparison with estimation from the work of Bolgar *et al.* [4]

4.2.2 NdB_4

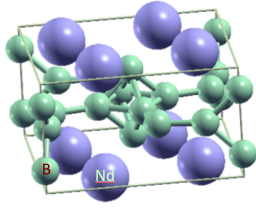


Figure 4.7: Unit cell of NdB_4 phase

- A: 7.1775 Å
- B: 7.1775 Å
- C: 4.0996 Å

The NdB_4 ground state crystal structure is a distorted structure from the simple cubic structures of NdB_6 . Both the Nd atom and octahedral B sublattices are distorted, introducing B atom pairs between the distorted Nd sublattices, shown in Figure 4.7.

The initial atomic positions and lattice parameters are taken from the work of Salamakha *et al.* [75] on the single crystal X-ray diffraction of NdB_4 . The ground state tetragonal crystal structure has the space group $P4/mbm$, and the unit cell contains $Z = 4$ formula units. The initial lattice parameters are:

These values do not significantly change after geometry optimization. As with NdB_6 , the single Hubbard site is determined to have a U_{eff} correction value of 5.7931 eV. The results of the calculations are shown in Table 4.2.

GGA+U calculation values provides good agreement with the experimental work of Meschel and Kleppa [61] using direct synthesis calorimetry. The order of agreement with experimental data is comparable to that of the same result for NdB_6 . This result shows the validity of the method used in this work to calculate the enthalpy of formation.

Phase	Total Energy [Ry]	Z	x	Calculation
NdB ₄	-2333.49114589	4	1	-583.37278647
Nd	-2149.35042903	4	1	-537.33760726
B	-137.51578368	12	4	-45.83859456
E _{form} [Ry]				-0.19658465
E _{form} , GGA+U [kJ/mol.atom]				-51.61328937
Expt. [kJ/mol.atom] [61]				53.3 ± 1.5
E _{form} , GGA [kJ/mol.atom]				-56.48200298

Table 4.2: NdB₄ Formation Enthalpy

Watanuki *et al.* [76] performed C_p measurement for the very low temperature region, showing several successive magnetic ordering transitions at $T = 4.8$ K, $T = 7.0$ K, and $T = 17.2$ K. These transitions lend credence to the hypothesis that NdB₄ possesses multipolar magnetic ordering, a state recently confirmed in another study on NdB₄. [64] Again, these transitions due to electronic contribution are not reflected in the phonon calculation results.

As with NdB₆, Bolgar *et al.* also fitted an enthalpy measurement with the Mayer-Kelly equation for 298.15 K $< T < 2307$ K. The equation for NdB₄ reads:

$$C_p(T) = 0.021044T + 116.55 - \frac{4454762}{T^2} \quad (4.3)$$

This function agrees well with the estimation of NdB₄ heat capacity from an earlier work [77].

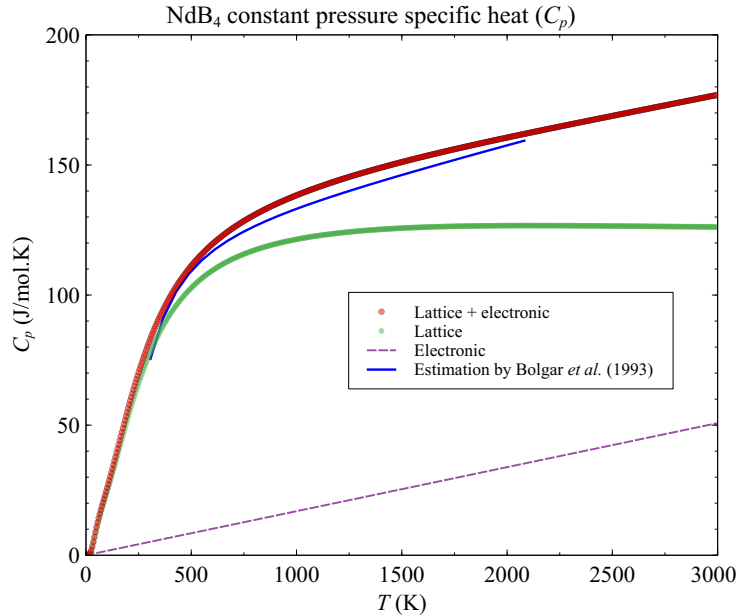


Figure 4.8: C_p from phonon calculation of NdB₄, in comparison with estimation from the work of Bolgar *et al.* [4]

Again, it shows a marked difference to the phonon calculation results for the high-temperature region, displayed in Figure 4.8. As with NdB₆, the results of our work is chosen for CALPHAD use.

4.2.3 Nd₂B₅

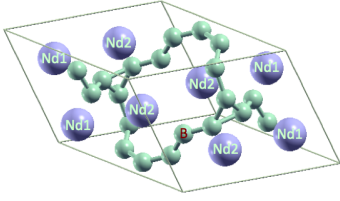


Figure 4.9: Unit cell of Nd₂B₅ phase

The binary phase Nd₂B₅ ground state crystal structure possesses the space group $C2/c$, with monoclinic crystal structure, based on the prototype structure Pr₂B₅. From the basic crystallographic data, a primitive cell was made and geometry optimization was run, resulting in lattice parameters of:

$$\begin{aligned} A: 8.3670 \text{ \AA} & & \alpha: 72.845^\circ \\ B: 8.3670 \text{ \AA} & & \beta: 107.155^\circ \\ C: 7.2841 \text{ \AA} & & \gamma: 128.635^\circ \end{aligned}$$

containing $Z = 4$ formula units per cell.

There are 2 inequivalent Wyckoff positions inhabited by Nd atoms, referred to in Figure 4.9 as Nd1 and Nd2. Effective Hubbard U correction U_{eff} parameter was self-consistently determined per the methods outlined in Chapter 2.1.2, resulting in U_{eff} values of:

$$\begin{aligned} \text{Nd1: } & 5.2099 \text{ eV} \\ \text{Nd2: } & 5.0492 \text{ eV} \end{aligned}$$

However, compared to other binary Nd-B compounds NdB₆ and NdB₄, experimental data on Nd₂B₅ are relatively scarce. Only the enthalpy of formation information is readily available, from direct synthesis calorimetry by Meschel and Kleppa. [62] This value, along with first-principles GGA+ U calculation, is shown in Table 4.3.

Phase	Total Energy [Ry]	Z	x	Calculation
Nd ₂ B ₅	-4528.94730505	4	1	-1132.23682626
Nd	-2149.34493787	4	2	-1074.67246894
B	-137.51536897	12	5	-57.29807040
E_{form} [Ry]				-0.26628692
E_{form} , GGA+ U [kJ/mol.atom]				-49.93829695
Expt. [kJ/mol.atom] [62]				-38.9 ± 1.9

Table 4.3: Nd₂B₅ Formation Enthalpy

The calculated formation enthalpy differs more than 10 kJ/mol.atom than the available experimental results. This discrepancy suggests that GGA+ U first-principles assessment of formation enthalpy is not reliable for Nd₂B₅ for the purposes of application in CALPHAD. This discrepancy is further discussed in Chapter 5.

To our knowledge, there are no experimental data available of C_p for Nd₂B₅. The results of the phonon calculation are displayed in Figure 4.10. As such, without any sort of comparison to test its validity, there can be no conclusive statements made about its reliability of this C_p calculation.

For CALPHAD application, it might be necessary to adjust its weight as input data to the optimization results, both in the binary and ternary levels. The similar results have been obtained in the recent DFT calculations for the Nd-B binary system by Colinet and Tedenac [78], as well as for isostructural Gd₂B₅ investigated in the same work. This discrepancy between

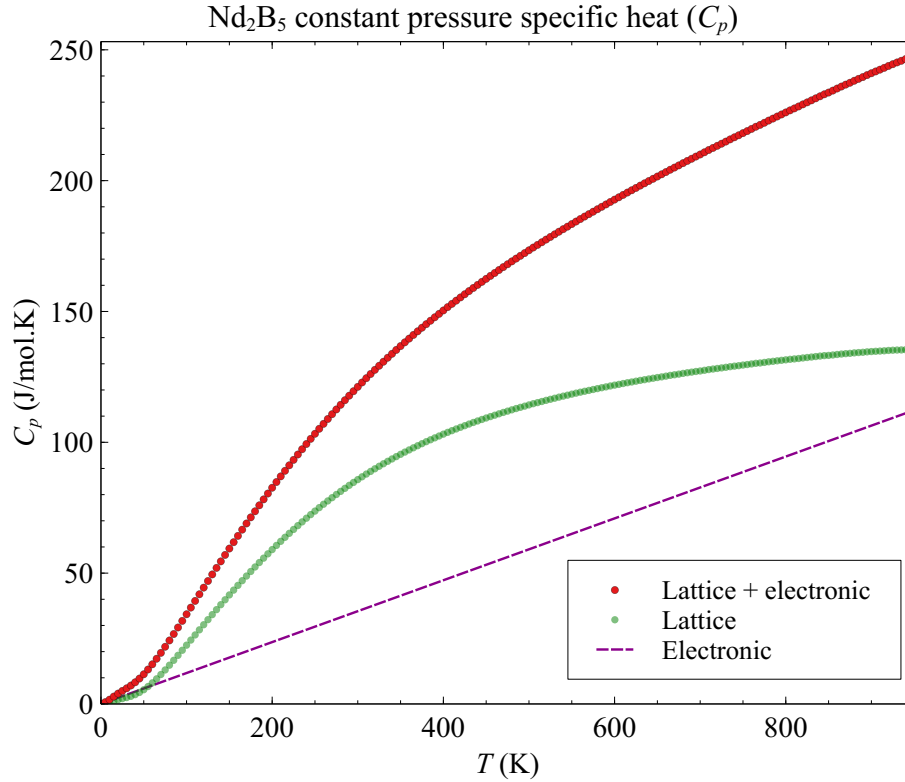


Figure 4.10: C_p from phonon calculation of Nd_2B_5

experimental and DFT results suggests a characteristic of the $R_2\text{B}_5$ structure which is not being captured by either GGA or GGA+ U calculations. As such, the CALPHAD optimization is performed by classifying Nd_2B_5 enthalpy of formation and C_p as outlier data and zero weight is added in the optimization.

4.2.4 $\text{Nd}_2\text{Fe}_{17}$

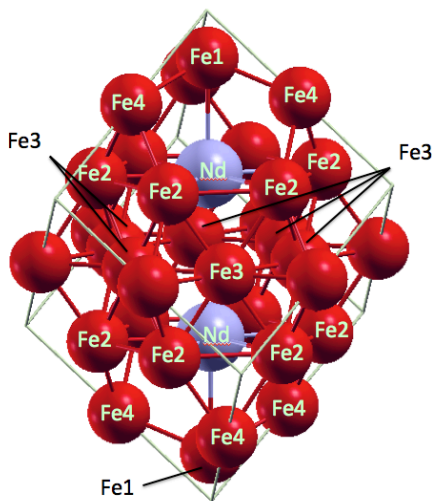


Figure 4.11: Unit cell of $\text{Nd}_2\text{Fe}_{17}$ phase

As one of only two stable binary compounds in the Nd-Fe system (the other being the relatively recently discovered $\text{Nd}_5\text{Fe}_{17}$ [57]), $\text{Nd}_2\text{Fe}_{17}$ is highly important to model this binary system.. The ground state crystal structure possesses the space group $R\bar{3}m$, with $\text{Th}_2\text{Zn}_{17}$ being the prototype crystal structure. As such, the crystal coordinates and Wyckoff positions follow those of $\text{Th}_2\text{Fe}_{17}$, while the initial lattice parameters are taken from the work of Long *et al.* [79] The unit cell contains $Z = 3$ formula units.

From the initial parameters, a rhombohedral primitive cell was found with $Z = 1$ formula unit inside. Geometry optimization produces lattice parameters as follows:

$$\begin{array}{ll} A: 6.4733 \text{ \AA} & \alpha: 83.012^\circ \\ B: 6.4733 \text{ \AA} & \beta: 83.012^\circ \end{array}$$

C: 6.4733 Å γ : 83.012°

from initial lattice parameters found in the work of Long *et al.* [79]

Nd occupies one Wyckoff position, while four other inequivalent positions are occupied by Fe. Five Hubbard sites in total are within the simulation cell.

Nd1: 5.6000 eV
 Fe2: 3.0130 eV
 Fe3: 3.1539 eV
 Fe4: 3.0244 eV
 Fe5: 2.9752 eV

These values are used in the GGA+U calculations of formation energy. The calculation is outlined in Table 4.4.

Phase	Total Energy [Ry]	Z	x	Calculation
Nd ₂ Fe ₁₇	-6672.35190026	1	1	-6672.35190026
Nd	-2149.34082403	4	2	-1074.67041201
Fe	-329.27248982	1	17	-5597.63232694
E_{form} [Ry]				-0.18721116
$E_{\text{form, GGA+U}}$ [kJ/mol.atom]				-3.39665762
Expt. [kJ/mol.atom] [80]				-3.0 ± 3.9

Table 4.4: Nd₂Fe₁₇ Formation Enthalpy

Phonon calculation results are displayed in Figure 4.12. The enthalpy of formation obtained agrees relatively well with the available experimental measurement by Meschel and Kleppa [80]. There is, however, little to no information regarding the experimentally measured C_p for Nd₂Fe₁₇.

4.3 Ternary phases

As previously mentioned, three stable compounds so far have been discovered in the Nd-Fe-B ternary system, which are the vital T1 (Nd₂Fe₁₄B) phase, T2 (Nd_{1.1}Fe₄B₄), and the T3 (Nd₅Fe₂B₆) phase. The T2 and T3 phases in particular present a challenge due to its relatively scarce information available. Multiple metastable states have been proposed for this ternary system, and while modelling them may be relevant to investigate certain thermodynamic phenomena or phase transitions in the Nd-Fe-B ternary system, generally speaking the three stable phases should take priority in any assessment.

A similar equation is used to obtain the formation enthalpy from the ternary phase. As with Equation (4.1), it subtracts the total energies of the ground state unary phases from the ternary phase. For the ternary phase A_xB_yC_z,

$$E_{\text{form}} = E_{\text{A}_x\text{B}_y\text{C}_z} - xE_{\text{A}} - yE_{\text{B}} - zE_{\text{C}} \quad (4.4)$$

the molar fractions $x, y,$ and z are collectively referred to as x . Each total energy is of one formula unit $Z = 1$. The formation enthalpy obtained is converted to the units [kJ/mol.atom].

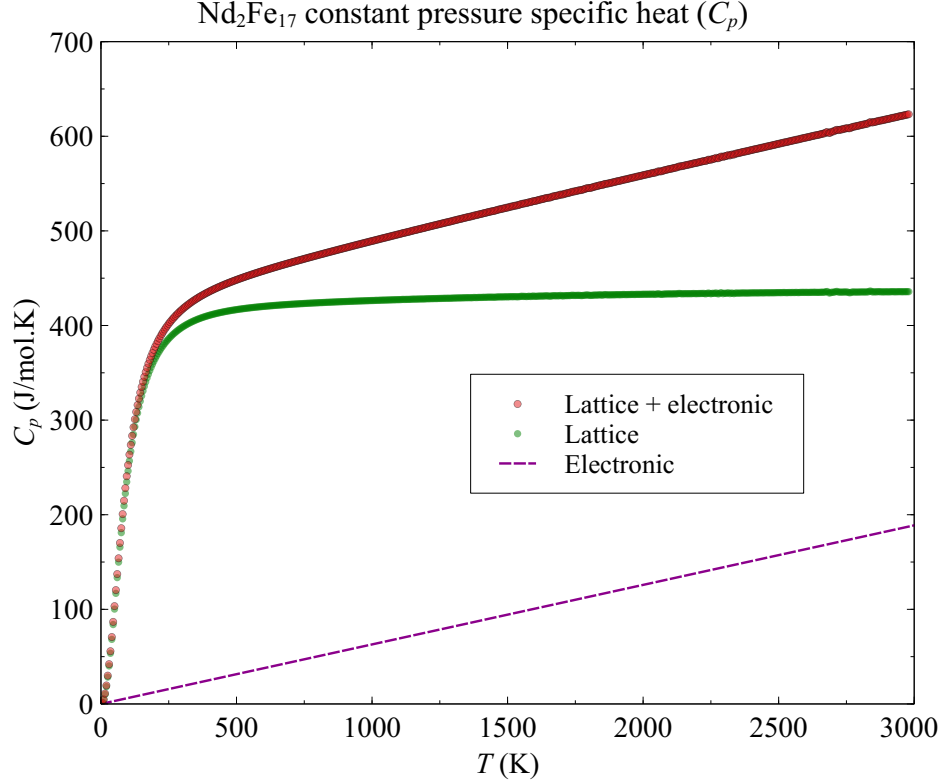


Figure 4.12: C_p from phonon calculation of $\text{Nd}_2\text{Fe}_{17}$

4.3.1 $\text{Nd}_5\text{Fe}_2\text{B}_6$

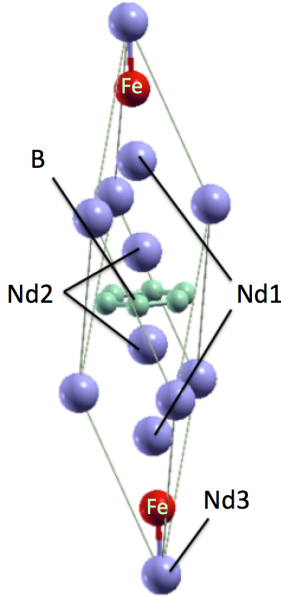


Figure 4.13: Unit cell of $\text{Nd}_5\text{Fe}_2\text{B}_6$ phase

The $\text{Nd}_5\text{Fe}_2\text{B}_6$ or T3 phase has the ground state crystal structure of the space group $R\bar{3}m$, and as such a rhombohedral primitive cell can be constructed (with $Z = 1$). Initial ground state crystal structure is taken from the work of Buschow *et al.* [81] and optimized, resulting in the following primitive cell:

$$\begin{array}{ll} A: 8.6834 \text{ \AA} & \alpha: 36.658^\circ \\ B: 8.6834 \text{ \AA} & \beta: 36.658^\circ \\ C: 8.6834 \text{ \AA} & \gamma: 36.658^\circ \end{array}$$

This primitive cell is shown in Figure 4.13.

A total of 4 Hubbard sites are present in the cell, with 3 inequivalent Nd atom positions and a single position occupied by the Fe atoms.

$$\begin{array}{l} \text{Nd1: } 5.6556 \text{ eV} \\ \text{Nd2: } 5.3697 \text{ eV} \\ \text{Nd3: } 5.3833 \text{ eV} \\ \text{Fe : } 4.9680 \text{ eV} \end{array}$$

used in the GGA+U calculations for formation enthalpy. The formation enthalpy calculation is detailed in Table 4.5.

Phase	Total Energy [Ry]	Z	x	Calculation
Nd ₅ Fe ₂ B ₆	-3414.35007388	1	1	-3414.35007388
Nd	-2149.27878747	4	5	-2686.59848434
Fe	-329.27190272	1	2	-658.54380544
B	-137.51932421	12	6	-68.75966211
E _{form} [Ry]				-0.44812199
E _{form} , GGA+U [kJ/mol.atom]				-44.68669291

Table 4.5: Nd₅Fe₂B₆ Formation Enthalpy

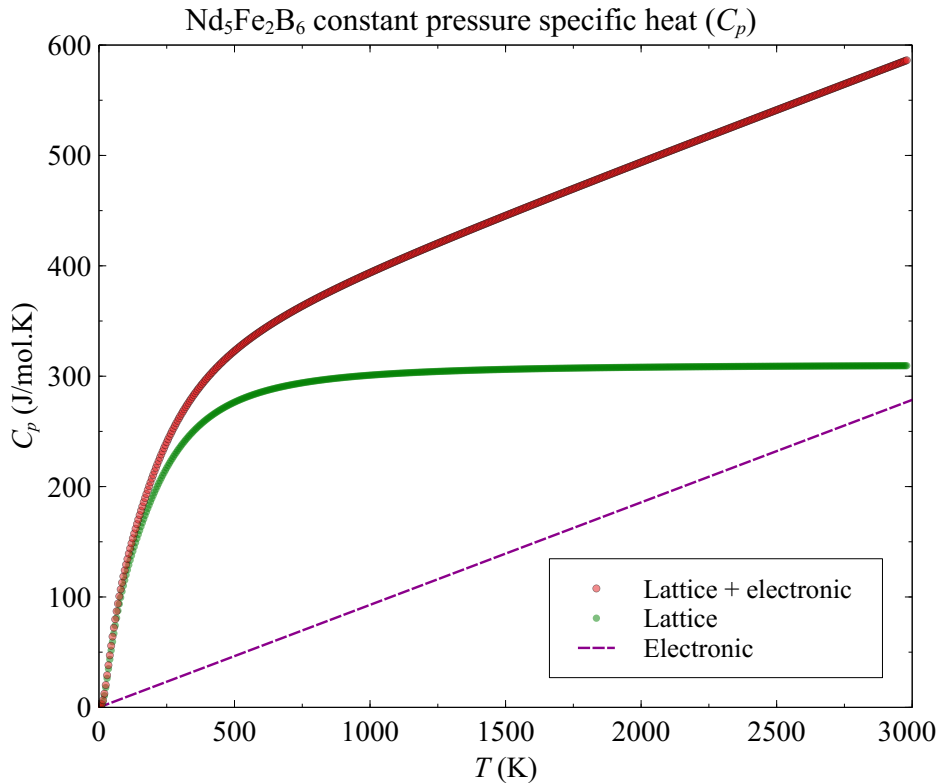


Figure 4.14: C_p from phonon calculation of Nd₅Fe₂B₆

Phonon calculation results are displayed in Figure 4.14. Neither formation enthalpy nor specific heat measurements of this phase are available as comparison, and as such, care must be taken to weigh these data appropriately to well model the proper Nd-rich corner of the ternary phase diagram.

4.4 CALPHAD assessment

CALPHAD assessment was performed for the binary Nd-B system using obtained thermodynamic data for compounds NdB₄ and NdB₆. The R-K polynomial coefficients were optimized with the PARROT module according to the enthalpy of formation and C_p theoretical predictions described in this chapter. The optimized Gibbs energy models give rise to the calculated phase diagram in Figure 4.16.

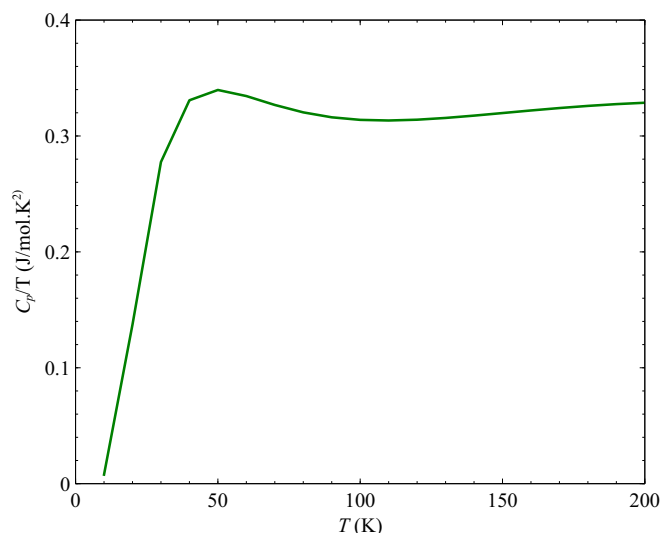


Figure 4.15: Calculated C_p/T plot for NdB_6 . An unusual peak is seen around $T = 50$ K, followed by the more expected linear section.

The results of the assessment of Chen *et al.* [53] which solely utilized available experimental data were used as a good starting point for the Gibbs energy parameters. These parameters were further optimized, resulting in the displayed phase diagram, taking advantage of both experimental and *ab initio* results.

Several issues emerged during our re-optimization, most notably due to the Schottky-like anomaly present in the C_p data for binary Nd-B compounds, seen in Figure 4.6 more detail in the C_p/T plot in Figure 4.15 for NdB_6 . The Schottky anomaly is unlikely to be the cause of this broad peak, due to the cause of Schottky anomalies (entropy of spin populations in magnetic materials) are unaccounted in the lattice vibrations. A similar anomaly can be seen for the case of YB_6 [82], however, which suggests that the same cause of the phenomena occurs in NdB_6 as well. In both materials there is large dependence of lattice volume on low temperature phonon modes, leading to the broad peak seen in Figure 4.15

This, coupled with the peak in C_p due to low temperature magnetic ordering shift, led to the impossibility to fit the C_p data of either NdB_6 and NdB_4 for $0 < T < 3000$ K, as is usually done with specific heat measurements. C_p data of NdB_6 fitted to a function from $300 < T < 3000$ K instead, and subsequently used to optimize directly the entropic term for the Gibbs energy models for NdB_6 .

Our results do not differ much from that of our initial starting point for optimization from Chen *et al.* [53], with the significant exception for the area of the plot around NdB_6 and NdB_4 , to which we have applied the enthalpy of formation and C_p data from our calculation. Regardless, our results have shown that *ab initio* results from DFT+U can be used to optimize the Gibbs energy models for the Nd-B binary system.

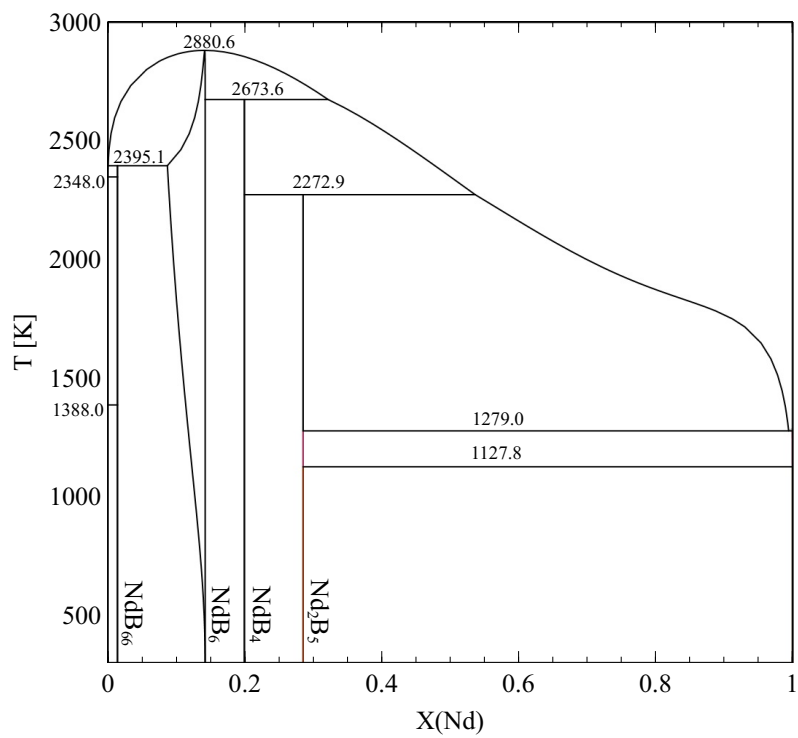


Figure 4.16: Calculated phase diagram of the Nd-B binary system for $T > 300$ K, utilizing *ab initio* calculation results in this work

Chapter 5

Conclusion

Thermodynamic properties of some of Nd-Fe-B constituent phases have been obtained from first-principles assessment in order to further CALPHAD assessment of the ternary system. Two thermodynamic properties are of interest for application in CALPHAD: the standard enthalpy of formation and the specific heat under constant pressure or C_p . Enthalpy of formation was obtained from DFT+U self-consistent calculations done with plane-wave basis set and the GGA-PBE exchange correlation functional. The effective Hubbard U correction is employed for valence electrons in localized $3d$ and $4f$ orbitals, and the parameter for this correction is determined self-consistently from first-principles [1].

C_p is obtained from phonon calculations of the constituent phases, using DFT as a atomic force calculator from finite displacements of atomic sites (the frozen phonon approach). The Quasi Harmonic Approximation (QHA) were employed over several values of unit cell volumes, leading to calculation of C_p . First-principle calculation methods are detailed in Chapter 2.

Phase	Formation Enthalpy [J/mol.atom]	
	E_{form}	Expt. data
NdB ₆	-45019	-46750 ± 1500
NdB ₄	-51613	-53300 ± 1500
Nd ₂ B ₅	-49938	-38900 ± 1900
Nd ₂ Fe ₁₇	-3397	-3000 ± 3900
Nd ₅ Fe ₂ B ₆	-44687	–

Table 5.1: Summary of formation enthalpies E_{form} obtained from first-principle calculations, with available experimental results for comparison

For both NdB₆ and NdB₄ binary phases, formation enthalpies were obtained with regular DFT (GGA-PBE) as well as the GGA+U correction. The Hubbard correction, in both cases, brought formation enthalpy values closer in agreement to experimental values, as shown in Tables 4.1 and 4.2. While a marked improvement over non-corrected GGA is evident, the Hubbard correction may not lead to better relative energetics for every compound. An example is an earlier work by Jain *et al.* [83] for the Fe-P-O phase diagram, in which neither GGA nor GGA+U alone correctly produces formation enthalpies. A mixing of the two results was performed which reduced the error significantly, but with the drawback of introducing empirical data to the method, limiting its predictive capability.

The differing values of U_{eff} used within the calculation of enthalpies of formation in this work stems from the application of the choice to use the linear response method of Cococcioni and de Gironcoli [1], which implies that different U_{eff} -values are appropriate for different compounds. While the conventional usage of the Hubbard U correction usually involves a uniform (equal) value of U term for traditional uses of DFT+ U , adherence to the initial scheme seems appropriate (accounting for the different chemical environments of each Hubbard site), especially when the work of Jain *et al.* [83] supports mixing of energies with regular GGA ($U_{\text{eff}} = 0$ eV).

GGA+ U calculation results obtained in this work mostly correspond well with available experimental data. An exception appeared for the binary Nd_2B_5 phase, for which there is a 10 kJ/mol.atom difference between the experimental determination of Meschel and Kleppa [62] using direct synthesis calorimetry and this calculation. The cause for the large discrepancy is not conclusively determined. Previous works with GGA exchange correlation potential also show this large discrepancy [78,84,85], and GGA+ U method used in this work does not rectify this discrepancy. Previous semi-empirical estimation of Nd_2B_5 with Miedema's method has also failed to reach agreement with this measurement.

One interesting observation to bring up is that the discrepancy also exists for Gd_2B_5 , which possesses the same crystal structure as Nd_2B_5 . [78] The reason for the discrepancy seems to be more related to the property of the crystal structure that is not captured by either GGA or GGA+ U method. Another possibility is that the direct synthesis calorimetry used to measure the enthalpy of formation for both compounds was inaccurate. However, this is considered unlikely as the same work was used to establish the enthalpy of formation for NdB_4 as well, which tracks very well with *ab initio* results. [62] As a result, specifically the *ab initio* results for Nd_2B_5 were subsequently treated as outliers in the CALPHAD assessment, and thus weighted at zero in the Gibbs energy model optimization.

For the high-temperature regions, the estimation from the work of Bolgar *et al.* [4] disagrees with the results of calculations for NdB_6 and NdB_4 . This discrepancy, illustrated in Figures 4.6 and 4.8, serves to highlight the improvements possible with *ab initio* methods over previous theoretical approximations and assumptions. It should be noted that Bolgar's estimation for NdB_6 conflicts with measurement done by Reiffers *et al.* [63], with which the phonon calculation results presented in Chapter 4.2.1 achieves better agreement around $T = 300$ K.

Due to C_p peaks at lower temperature, the fitting of C_p data was not performed as it is usually performed. Instead, the data from $300 < T < 3000$ K is used as opposed to the fitting of low temperature data as well. The magnetic ordering shift, as well as the broad peak corresponding to anomaly also encountered in YB_6 , leads to difficulty in fitting the higher temperature region to match the low temperature functions. In this way, the *ab initio* calculated thermodynamic data of NdB_6 and NdB_4 by GGA+ U method were successfully used in a reoptimization of the Gibbs energy models for the binary Nd-B system, producing the reassessed phase diagram in Figure 4.16. This is the first time such *ab initio* calculation results have been successfully used for the Nd-B system CALPHAD reoptimization scheme.

Bibliography

- [1] M. Cococcioni and S. de Gironcoli, “Linear response approach to the calculation of the effective interaction parameters in the LDA+U method,” *Phys. Rev. B*, vol. 71, p. 035105, 2005.
- [2] M. A. van Ende and I. H. Jung, “Critical thermodynamic evaluation and optimization of the fe-b, fe-nd, b-nd, and nd-fe-b systems,” *J. Alloys Compd.*, vol. 548, pp. 133–154, 2013.
- [3] B. Hallemans, P. Wollants, and J. R. Roos, “Thermodynamic Assessment of the Fe-Nd-B Phase Diagram,” *J. Phase Equib.*, vol. 16, pp. 137–149, 1995.
- [4] A. S. Bolgar, V. B. Muratov, A. V. Blinder, A. I. Kryklya, and A. P. Suodis, “Thermodynamic properties of the rare earth borides and carbides in a wide temperature range,” *J. Alloys Compd.*, vol. 201, pp. 127–128, 1993.
- [5] H. L. Lukas, S. G. Fries, and B. Sundman, *Computational Thermodynamics: The Calphad Method*. Cambridge University Press, 2007.
- [6] M. Sagawa, S. Hirosawa, H. Yamamoto, S. Fujimura, and Y. Matsuura, “Nd-Fe-B Permanent Magnet Materials,” *Jpn. H. Appl. Phys.*, vol. 26, p. 785, 1987.
- [7] P. Tenaud, H. Lemaire, and F. Vial, “Recent improvements in NdFeB sintered magnets,” *J. Magn. Magn. Mater.*, vol. 101, pp. 328–332, 1991.
- [8] D. S. Sholl and J. A. Steckel, *Density Functional Theory: A Practical Introduction*. Wiley, 2009.
- [9] A. Jacob, C. Schmetterer, L. Singheiser, A. Gray-Weale, B. Hallstedt, and A. Watson, “Modeling of Fe-W phase diagram using first principles and phonons calculations,” *Calphad*, vol. 50, pp. 92–104, 2015.
- [10] B. Hallemans, P. Wollants, and J. Roos, “Thermodynamic reassessment and calculation of the Fe-B phase diagram,” *Zeitschrift für metallkunde*, vol. 85, pp. 676–682, 1994.
- [11] T. V. Rompaey, K. C. H. Kumar, and P. Wollants, “Thermodynamic optimization of the B-Fe system,” *J. Alloys Compd.*, vol. 334, pp. 173–181, 2002.
- [12] K. Hongo, N. T. Cuong, and R. Maezono, “The Importance of Electron Correlation on Stacking Interaction of Adenin-Thymine Base-Pair Step in B-DNA: A Quantum Monte Carlo Study,” *J. Chem. Theory Comput.*, vol. 9, no. 2, pp. 1081–1086, 2013.
- [13] K. S. Qin, T. Ichibha, K. Hongo, and R. Maezono, “Inconsistencies in *ab initio* evaluations of non-additive contributions of DNA stacking energies,” *Chem. Phys.*, vol. 529, p. 110554, 2020.

- [14] P. Hohenberg and W. Kohn, “Inhomogeneous Electron Gas,” *Phys. Rev.*, vol. 136, no. 3B, pp. B864–B871, 1964.
- [15] W. Kohn and L. J. Sham, “Self-Consistent Equations Including Exchange and Correlation Effects,” *Phys. Rev.*, vol. 140, no. 4A, pp. A1133–A1138, 1965.
- [16] H. J. Monkhorst and J. D. Pack, “Special points for brillouin-zone integrations,” *Phys. Rev. B*, vol. 13, p. 5188, 1976.
- [17] N. Marzari, D. Vanderbilt, A. D. Vita, and M. C. Payne, “Thermal contraction and disordering of the al(110) surface,” *Phys. Rev. Lett.*, vol. 82, p. 3296, 1999.
- [18] D. R. Hamann, M. Schlüter, and C. Chiang, “Norm-conserving pseudopotentials,” *Phys. Rev. Lett.*, vol. 43, pp. 1494–1497, 1979.
- [19] L. Kleinman and D. M. Bylander, “Efficacious form for model pseudopotentials,” *Phys. Rev. Lett.*, vol. 48, pp. 1425–1428, 1982.
- [20] P. E. Blöchl, “Projector augmented-wave method,” *Phys. Rev. B*, vol. 50, p. 17953, 1994.
- [21] G. Kresse and D. Joubert, “From ultrasoft pseudopotentials to the projector augmented-wave method,” *Phys. Rev. B*, vol. 59, p. 1758, 1999.
- [22] J. P. Perdew and A. Zunger, “Self-consistent equations including exchange and correlation effects,” *Phys. Rev. B*, vol. 23, pp. 5048–5079, 1981.
- [23] J. P. Perdew, K. Burke, and M. Ernzerhof, “Generalized gradient approximation made simple,” *Phys. Rev. Lett.*, vol. 77, p. 3865, 1996.
- [24] S. L. Dudarev, G. A. Botton, S. Y. Savrasov, C. J. Humphreys, and A. P. Sutton, “Electron-energy-loss spectra and the structural stability of nickel oxide: An LSDA+U study,” *Phys. Rev. B*, vol. 57, pp. 1505–1509, 1998.
- [25] M. Lazzeri, C. Attaccalite, L. Wirtz, and F. Mauri, “Impact of the electron-electron correlation on phonon dispersion: Failure of LDA and GGA DFT functionals in graphene and graphite,” *Phys. Rev. B*, vol. 78, p. 081406(R), 2008.
- [26] M. Sagawa, S. Hirosawa, H. Yamamoto, S. Fujimura, and Y. Matsuura, “Cu₂ZnSnS₄ as a potential photovoltaic material: A hybrid Hartree-Fock density functional theory study,” *Jpn. H. Appl. Phys.*, vol. 26, p. 785, 1987.
- [27] J. Hubbard, “Electron correlations in narrow energy bands,” *Proc. Math. Phys.*, vol. 276, no. 1365, pp. 238–257, 1963.
- [28] V. I. Anisimov, J. Zaanen, and O. K. Andersen, “Band theory and Mott insulators: Hubbard *U* instead of Stoner *I*,” *Phys. Rev. B*, vol. 44, pp. 943–954, 1991.
- [29] V. I. Anisimov, I. V. Solovyev, M. A. Korotin, M. T. Czyzyk, and G. A. Sawatzky, “Density-functional theory and NiO photoemission spectra,” *Phys. Rev. B*, vol. 48, no. 23, p. 16929, 1993.
- [30] V. I. Anisimov, F. Aryasetiawan, and A. I. Lichtenstein, “First-principles calculations of the electronic structure and spectra of strongly correlated systems: the LDA+*U* method,” *J. Phys. Condens. Matter*, vol. 9, pp. 767–808, 1997.

- [31] I. V. Solovyev and P. H. Dederichs, “Corrected atomic limit in the local-density approximation and the electronic structure of d impurities in Rb,” *Phys. Rev. B*, vol. 50, no. 23, p. 16861, 1994.
- [32] A. I. Liechtenstein, V. I. Anisimov, and J. Zaanen, “Density-functional theory and strong interactions: Orbital ordering in Mott-Hubbard insulators,” *Phys. Rev. B*, vol. 52, no. 8, p. R5467, 1995.
- [33] O. Gunnarsson, O. K. Andersen, O. Jepsen, and J. Zaanen, “Density-functional calculation of the parameters in the Anderson model: Application to mn in CdTe,” *Phys. Rev. B*, vol. 39, no. 3, p. 1708, 1989.
- [34] P. Giannozzi, S. Baroni, N. Bonini, M. Calandra, R. Car, C. Cavazzoni, D. Ceresoli, G. L. Chiarotti, M. Cococcioni, I. Dabo, A. D. Corso, S. Fabris, G. Fratesi, S. de Gironcoli, R. Gebauer, U. Gerstmann, C. Gougoussis, A. Kokalj, M. Lazzeri, L. Martin-Samos, N. Marzari, F. Mauri, R. Mazzarello, S. Paolini, A. Pasquarello, L. Paulatto, C. Sbraccia, S. Scandolo, G. Sclauzero, A. P. Seitsonen, A. Smogunov, P. Umari, and R. M. Wentzcovitch, “Quantum espresso: a modular and open-source software project for quantum simulations of materials,” *J. Phys. Condens. Matter*, vol. 21, p. 395502, 2009.
- [35] J. F. Janak, “Proof that $\partial E/\partial n_i = \epsilon_i$ in density-functional theory,” *Phys. Rev. B*, vol. 18, no. 12, p. 7165, 1978.
- [36] P. H. Dederichs, S. Blügel, R. Zeller, and H. Akai, “Ground States of Constrained Systems: Application to Cerium Impurities,” *Phys. Rev. Lett.*, vol. 53, no. 26, p. 2512, 1984.
- [37] T. Yanai, G. I. Fann, Z. Gan, and R. J. Harrison, “Multiresolution quantum chemistry in multiwavelet bases: Analytic derivatives for Hartree-Fock and density functional theory,” *J. Chem. Phys.*, vol. 121, p. 2866, 2004.
- [38] J. D. Head and M. C. Zerner, “A Broyden-Fletcher-Goldfarb-Shanno optimization procedure for molecular geometries,” *Chem. Phys. Lett.*, vol. 122, pp. 264–270, 1985.
- [39] A. Togo and I. Tanaka, “First principles phonon calculations in materials science,” *Scr. Mater.*, vol. 108, pp. 1–5, 2015.
- [40] G. Kresse and J. Hafner, “*Ab initio* molecular dynamics for liquid metals,” *Phys. Rev. B*, vol. 47, p. 558, 1993.
- [41] G. Kresse and J. Hafner, “*Ab initio* molecular dynamics simulation of the liquid-metal-amorphous-semiconductor transition in germanium,” *Phys. Rev. B*, vol. 49, p. 14251, 1994.
- [42] G. Kresse and J. Furthmüller, “Efficiency of *ab initio* total energy calculations for metals and semiconductors using a plane-wave basis set,” *Comput. Mat. Sci.*, vol. 6, p. 15, 1996.
- [43] G. Kresse and J. Furthmüller, “Efficient iterative schemes for *ab initio* total-energy calculations using a plane-wave basis set,” *Phys. Rev. B*, vol. 54, p. 11169, 1996.
- [44] F. Birch, “Finite Elastic Strain of Cubic Crystals,” *Phys. Rev.*, vol. 71, p. 809, 1947.
- [45] L. Kaufman, “The lattice stability of metals - I. Titanium and zirconium,” *Acta Metallurgica*, vol. 7, no. 8, pp. 575–587, 1959.

- [46] J. O. Andersson, T. Helander, L. Höglund, P. F. Shi, and B. Sundman, “Thermo-Calc and DICTRA, Computational tools for materials science,” *Calphad*, vol. 26, pp. 273–312, 2002.
- [47] A. Dinsdale, “SGTE Data for Pure Elements,” *Calphad*, vol. 15, pp. 317–425, 1991.
- [48] J. Tomiska, “Mathematical conversions of the thermodynamic excess functions represented by the Redlich-Kister expansion, and by the Chebyshev polynomial series to power series representations and vice-versa,” *Calphad*, vol. 8, pp. 283–294, 1984.
- [49] K. Girgis, M. Kraft, U. Weis, P. Fischer, and M. Sostarich, “Crystal and magnetic structure of the permanent magnet materials $\text{Nd}_2\text{Fe}_{14-x}\text{Co}_x\text{B}$ ($x = 0 - 14$),” *J. Less Common Met.*, vol. 162, pp. 335–342, 1990.
- [50] Y. Matsuura, S. Hirosawa, H. Yamamoto, S. Fujimura, M. Sagawa, and K. Osamura, “Phase diagram of the Nd-Fe-B ternary system,” *Jpn. J. Appl. Phys.*, vol. 24, no. 8A, p. L635, 1985.
- [51] V. Raghavan, “B-Fe-Nd (Boron-Iron-Neodymium),” *J. Phase Equilib.*, vol. 24, no. 5, pp. 451–454, 2003.
- [52] G. J. Zhou, Y. Luo, and Y. Zhou, “Thermodynamic reassessment of the Nd-Fe-B ternary system,” *J. Electron. Mater.*, vol. 45, no. 1, pp. 418–425, 2016.
- [53] T. L. Chen, J. Wang, C. P. Guo, C. R. Li, Z. M. Du, G. H. Rao, and H. Y. Zhou, “Thermodynamic description of the Nd-Fe-B ternary system,” *Calphad*, vol. 66, p. 101627, 2019.
- [54] E. K. Storms, “Phase Relationship, Vaporization, and Thermodynamic Properties of Neodymium Hexaboride,” *J. Phys. Chem.*, vol. 85, pp. 1536–1540, 1981.
- [55] K. Tanaka and T. Saito, “Phase equilibria in TiB_2 -reinforced high modulus steel,” *J. Phase Equilib.*, vol. 20, p. 207, 1999.
- [56] M. G. Poletti and L. Battezzati, “Assessment of the ternary Fe-Si-B phase diagram,” *Calphad*, vol. 43, pp. 40–47, 2013.
- [57] F. J. Landgraf, G. S. Schneider, V. Villas-Boas, and F. P. Missel, “Solidification and solid state transformations in Fe Nd: A revised phase diagram,” *J. Less Common Metals*, vol. 163, pp. 209–218, 1990.
- [58] F. J. Landgraf, F. P. Missel, G. Knoch, B. Grieb, and E.-T. Henig, “Binary Fe-Nd metastable phases in the solidification of Fe-Nd-B alloys,” *J. Applied Phys.*, vol. 70, pp. 6107–6109, 1991.
- [59] W. Zhang, G. Liu, and K. Han, “The Fe-Nd (Iron-Neodymium) System,” *J. Phase Equilib.*, vol. 13, pp. 645–648, 1992.
- [60] R. E. Aune and S. Seetharaman, “Experimental studies of heat capacities of $\text{Nd}_2\text{Fe}_{17}$, $\text{Nd}_2\text{Fe}_{17}\text{N}_{1.49}$, and $\text{Nd}_2\text{Fe}_{17}\text{N}_{1.75}$ alloys in the temperature range 273–773 K,” *High Temperature Materials and Processes (UK) (UK)*, vol. 17, pp. 299–311, 1998.
- [61] S. V. Meschel and O. J. Kleppa, “Standard Enthalpies of Formation of Some Borides of Ce, Pr, Nd, and Gd by High-Temperature Reaction Calorimetry,” *J. Alloys Compd.*, vol. 226, pp. 243–247, 1995.

- [62] S. V. Meschel and O. J. Kleppa, “Thermochemistry of Alloys of Transition Metals and Lanthanide Metals with Some IIIB and IVB Elements in the Periodic Table,” *J. Alloys Compd.*, vol. 321, pp. 183–200, 2001.
- [63] M. Reiffers, J. Šebek, E. Šantavá, N. Shitsevalova, S. Gabáni, G. Pristáš, and K. Flachbart, “Heat Capacity of NdB₆,” *J. Magn. Magn. Mater.*, vol. 310, pp. e595–e597, 2007.
- [64] H. Yamauchi, N. Metoki, R. Watanuki, K. Suzuki, H. Fukazawa, S. Chi, and J. A. Fernandez-Baca, “Magnetic structure and quadrupolar order parameter driven by geometrical frustration effect in ndb₄,” *J. Phys. Soc. Japan*, vol. 86, p. 044705, 2017.
- [65] A. Nakaue, “Studies on the pressure-temperature phase diagram of nd, sm, gd, and dy,” *J. Less Common Met.*, vol. 60, pp. 47–58, 1978.
- [66] R. M. Moon, J. W. Cable, and W. C. Koehler, “Magnetic structure of neodymium,” *J. Applied Phys.*, vol. 35, pp. 1041–1042, 1964.
- [67] R. Kohlhaas, P. Donner, and N. Schmitz-Pranghe, “Über die temperaturabhängigkeit der gitterparameter von eisen kobalt und nickel im bereich hoher temperaturen,” *Z. Angew. Phys.*, vol. 23, p. 245, 1967.
- [68] V. L. Moruzzi, J. F. Janak, and A. R. Williams, *Calculated Electronic Properties of Metals*. Pergamon Press, 1978.
- [69] G. W. Fernando, R. E. Watson, M. Weinert, A. N. Kocharian, A. Ratnaweera, and K. Tenakone, “Magnetic moment of iron in metallic environments,” *Phys. Rev. B*, vol. 61, no. 1, p. 375, 2000.
- [70] M. J. van Setten, M. A. Uijtewaal, G. A. de Wijs, and R. A. de Groot, “Thermodynamic stability of boron: The role of defects and zero point motion,” *J. Am. Chem. Soc.*, vol. 129, pp. 2458–2465, 2007.
- [71] S. Shang, Y. Wang, R. Arroyave, and Z. K. Liu, “Phase stability in α - and β -rhombohedral boron,” *Phys. Rev. B*, vol. 75, p. 092101, 2007.
- [72] G. Will and B. Kiefer, “Electron deformation density in rhombohedral α -boron,” *Z. Anorg. Allg. Chem.*, vol. 627, pp. 2100–2104, 2001.
- [73] C. M. McCarthy and C. W. Tompson, “Magnetic structure of ndb₆,” *J. Phys. Chem. Solids*, vol. 41, pp. 1319–1321, 1980.
- [74] H. Han, “Density-functional theory study of the effect of pressure on the elastic properties of cab₆,” *Chin. Phys. B*, vol. 22, p. 077101, 2013.
- [75] P. Salamakha, A. P. Gonçalves, O. Sologub, and M. Almeida, “Single crystal investigation of the binary ndb₄ compound,” *J. Alloys Compd.*, vol. 316, pp. L4–L6, 2001.
- [76] R. Watanuki, T. Kobayashi, R. Noguchi, and K. Suzuki, “Possible multipolar transition in NdB₄,” *J. Phys. Conf. Ser.*, vol. 150, p. 042229, 2009.
- [77] O. H. Krikorian, *Estimation of Heat Capacities and Other Thermodynamic Properties of Refractory Borides*, vol. UCRL-51043. California Univ., Livermore, Lawrence Radiation Lab., 1971.

- [78] C. Colinet and J. C. Tedenac, “Enthalpies of formation of rare-earth borides from first principles and comparison with experimental values,” *Calphad*, vol. 62, pp. 49–60, 2018.
- [79] G. J. Long, G. K. Marasinghe, S. Mishra, O. A. Pringle, Z. Hu, W. B. Yelon, D. P. Middleton, K. H. J. Buschow, and F. Grandjean, “A magnetic, neutron diffraction, and mössbauer spectral study of the $\text{Nd}_2\text{Fe}_{17-x}\text{Al}_x$ solid solutions,” *J. Appl. Phys.*, vol. 76, p. 5383, 1994.
- [80] S. V. Meschel, P. Nash, Q. N. Gao, J. C. Wang, and Y. Du, “The standard enthalpies of formation of some binary intermetallic compounds of lanthanide-iron systems by high temperature direct synthesis calorimetry,” *J. Alloys Compd.*, vol. 554, pp. 232–239, 2013.
- [81] P. Deppe, M. Rosenberg, and K. H. J. Buschow, “A Mössbauer spectroscopy study of $\text{Nd}_5\text{Fe}_2\text{B}_6$,” *Solid state commun.*, vol. 64, pp. 1247–1251, 1987.
- [82] R. Lortz, Y. Wang, U. Tutsch, S. Abe, C. Meingast, P. Popovich, W. Knafo, N. Shitsevalova, Y. B. Paderno, and A. Junod, “Superconductivity mediated by a soft phonon mode: Specific heat, resistivity, thermal expansion, and magnetization of YB_6 ,” *Phys. Rev. B*, vol. 73, p. 024512, 2006.
- [83] A. Jain, G. Hautier, S. P. Ong, C. J. Moore, C. C. Fischer, K. A. Persson, and G. Ceder, “Formation enthalpies by mixing GGA and GGA+U calculations,” *Phys. Rev. B*, vol. 84, p. 045115, 2011.
- [84] J. E. Saal, S. Kirklin, M. Aykol, B. Meredig, and C. Wolverton, “Materials Design and Discovery with High-Throughput Density Functional Theory: The Open Quantum Materials Database (OQMD),” *JOM*, vol. 65, pp. 1501–1509, 2013.
- [85] S. Kirklin, J. E. Saal, B. Meredig, A. Thompson, J. W. Doak, M. Aykol, S. Rühl, and C. Wolverton, “The Open Quantum Materials Database (OQMD): assessing the accuracy of DFT formation energies,” *npj Comput. Mater.*, vol. 1, p. 15010, 2015.

Biography

Name	Mr. Adie Tri Hanindriyo
Date of Birth	23 November 1992
Educational Attainment	Master of Material Science: Japan Advanced Institute of Science and Technology, Ishikawa, Japan, 2018 Bachelor of Engineering: Bandung Institute of Technology, Bandung, Indonesia, 2015
Scholarship	2015-2018: Monbukagakusho (MEXT) Scholarship

Work Experiences

Publications

- [1] A.T. Hanindriyo, T.B.M.Y.Y. Prawira, M.K. Agusta, R. Maezono, H.K. Dipojono, “Computational Design of Ni-Zn Based Catalyst for Direct Hydrazine Fuel Cell Catalyst using Density Functional Theory” *Procedia Engineering*, vol. 170, p. 148-153, 2017
- [2] A.T. Hanindriyo, S. Sridar, K.C. Hari Kumar, K. Hongo, and R. Maezono, “*Ab initio* thermodynamic properties of certain compounds in Nd-Fe-B system” *Comp. Mat. Sci.*, vol. 180, p. 109696, 2020
- [3] A. Hermawan, A.T. Hanindriyo, E.R. Ramadhan, Y. Asakura, T. Hasegawa, K. Hongo, M. Inada, R. Maezono, and S. Yin, “Octahedral morphology of NiO with (111) facet synthesized from the transformation of NiOHCl for the NO_x detection and degradation: experiment and DFT calculation” *Inorg. Chem. Front.*, vol. 7, p. 3431-3442, 2020
- [4] T. Hasegawa, A. Shigee, Y. Nishiwaki, M. Nagasako, A.T. Hanindriyo, K. Hongo, R. Maezono, T. Ueda, and S. Yin, “New layered perovskite family built from [CeTa₂O₇]⁻ layers: coloring mechanism from unique multi-transitions” *Chem. Commun.*, vol. 56, p. 8591-8594, 2020
- [5] A. Raghav, A.T. Hanindriyo, K. Utimula, M. Abbasnejad, R. Maezono, and E. Panda “Intrinsic electronic defect states of anatase using density functional theory” *Comp. Mat. Sci.*, vol. 184, p. 109925, 2020